An anchor-tether 'hindered' HCN1 inhibitor is antihyperalgesic in a rat spared nerve injury neuropathic pain model

Gareth R. Tibbs[1], Rajendra Uprety[2], J. David Warren[3], Nicole P. Beyer[1], Rebecca L. Joyce[1], Matthew A. Ferrer[1], Wilfredo Mellado[4], Victor S. C. Wong[4], David C. Goldberg[4], Melanie W. Cohen[4], Christopher J. Costa[4], Zhucui Li[3], Guoan Zhang[3], Noah E. Dephoure[3,5], Dipti N. Barman[3], Delin Sun[6], Helgi I. Ingólfsson[6], Anthony A. Sauve[2,†], Dianna E. Willis[4,7,*] and Peter A. Goldstein[1,7,8,*]

[1]Department of Anesthesiology, Weill Cornell Medicine, New York, NY, USA, [2]Department of Pharmacology, Weill Cornell Medicine, New York, NY, USA, [3]Department of Biochemistry, Weill Cornell Medicine, New York, NY, USA, [4]Burke Neurological Institute, White Plains, NY, USA, [5]Sandra and Edward Meyer Cancer Center, Weill Cornell Medicine, New York, NY, USA, [6]Lawrence Livermore National Laboratory, Livermore, CA, USA, [7]Feil Family Brain & Mind Research Institute, Weill Cornell Medicine, New York, NY, USA and [8]Department of Medicine, Weill Cornell Medicine, New York, NY, USA

*Corresponding authors. E-mails: diw2004@med.cornell.edu, pag2014@med.cornell.edu
†Deceased.

Abstract

Background: Neuropathic pain impairs quality of life, is widely prevalent, and incurs significant costs. Current pharmacological therapies have poor/no efficacy and significant adverse effects; safe and effective alternatives are needed. Hyperpolarisation-activated cyclic nucleotide-regulated (HCN) channels are causally implicated in some forms of peripherally mediated neuropathic pain. Whilst 2,6-substituted phenols, such as 2,6-di-*tert*-butylphenol (26DTB-P), selectively inhibit HCN1 gating and are antihyperalgesic, the development of therapeutically tolerable, HCN-selective antihyperalgesics based on their inverse agonist activity requires that such drugs spare the cardiac isoforms and do not cross the blood−brain barrier.

Methods: *In silico* molecular dynamics simulation, *in vitro* electrophysiology, and *in vivo* rat spared nerve injury methods were used to test whether 'hindered' variants of 26DTB-P (wherein a hydrophilic 'anchor' is attached in the *para*-position of 26DTB-P *via* an acyl chain 'tether') had the desired properties.

Results: Molecular dynamics simulation showed that membrane penetration of hindered 26DTB-Ps is controlled by a tethered diol anchor without elimination of head group rotational freedom. *In vitro* and *in vivo* analysis showed that BP4L-18:1:1, a variant wherein a diol anchor is attached to 26DTB-P *via* an 18-carbon tether, is an HCN1 inverse agonist and an orally available antihyperalgesic. With a CNS multiparameter optimisation score of 2.25, a >100-fold lower drug load in the brain *vs* blood, and an absence of adverse cardiovascular or CNS effects, BP4L-18:1:1 was shown to be poorly CNS penetrant and cardiac sparing.

Conclusions: These findings provide a proof-of-concept demonstration that anchor-tethered drugs are a new chemotype for treatment of disorders involving membrane targets.

Keywords: antihyperalgesia; HCN1; ion channel; nerve injury; neuropathic pain; rat

Chronic pain impairs an individual's quality of life, is widely prevalent, and has significant economic cost. In the United States alone, at least 116 million adults suffer from chronic pain; the associated costs exceed $500 billion per year[1]; in Europe, nearly 20% of the population lives with chronic pain, and direct and indirect costs associated with chronic pain consume 3–10% of gross domestic product.[2] Neuropathic pain (chronic pain arising from aberrant activity in neurones themselves) accounts for 18% of patients with chronic pain.[3] Neuropathic pain is commonly associated with diabetes mellitus, antineoplastic cancer treatment, peripheral nerve injury, and neurological disorders (such as stroke and multiple sclerosis).[4–6]

Pharmacological intervention is a mainstay for the treatment of neuropathic pain.[6] First-line therapy includes the use of the antidepressant duloxetine or the use of anti-epileptic $\alpha2$-δ ligands, such as gabapentin, although both have poor (or no) efficacy[7,8] and appreciable dose-limiting side-effects.[4–6] Whilst opioids are effective in relieving acute nociceptive pain, they are of little use in the treatment of neuropathic pain,[9–15] and their inappropriate use has contributed to the global opioid crisis.[16–19] Thus, there is a critical need for the development of safe, effective antihyperalgesics.

Sensory neurone hyperexcitability drives the development of neuropathic pain. Attempts to limit such aberrant excitability *via* inhibition of voltage-gated sodium and calcium channels[20] have not resulted in translation to approved therapeutics. Whilst hyperpolarisation-activated cyclic nucleotide-regulated (HCN) channels have garnered interest as alternative targets[20–22] (particularly HCN1[23–26] and HCN2[27,28]), strategies to exploit HCN inhibitors need to surmount two significant hurdles. First, given the widespread expression of HCN2 (and HCN4) protein in human atrial and ventricular tissues[29,30] and HCN2 mRNA expression in sinoatrial and paranodal areas,[31] it is likely an HCN2 antagonist, even one highly-selective for HCN2 over HCN4, will incur unacceptable cardiac side effects. Second, the widespread distribution of all four HCN isoforms in the CNS Supplementary Fig. S1) suggests that significant penetration of

the blood–brain barrier (BBB) by inhibitors of *any* HCN isoform will lead to marked undesirable central side-effects. Given that HCN1 and HCN2 subunits freely co-assemble,[32] and co-assembled channels can inherit the pharmacological profile of the HCN1 parent subunit,[33] suggests that it is likely that targeting sensory neurone I_h with an HCN1-selective inhibitor[24–26] that does not cross the BBB will likely have the most desirable therapeutic profile.

We and others have shown that simple alkylphenols, such as 2,6-di-*iso*-propylphenol (26DIP-P) and 2,6-di-*tert*-butylphenol (26DTB-P), selectively inhibit gating of HCN1 channels[25,33,34] and relieve neuropathic pain, independently of central γ-aminobutyric acid type A (GABA$_A$) and spinal glycine receptor modulation.[25,35] Consistent with the structural characteristics of 26DIP-P binding to its cryogenic electron microscopy-determined general anaesthetic site in GABA$_A$ receptors,[36] alkylphenol association with HCN1 channels appears to be to a defined site on the lipid-facing outer shell of the channel pore.[34,37] We hypothesised that attachment of a 'tethered anchor' to the inhibitory, HCN1-selective, alkylphenol-derived pharmacophore (wherein the anchor consists of a hydrophilic moiety and the tether a flexible carbon-based chain) could limit molecule penetration of cell membranes and the BBB whilst permitting or even enhancing pharmacophore access to its inhibitory site *via* the plasma membrane.

Using a combination of *in silico* and *in vitro* approaches, we demonstrate that BP4L-18:1:1 (comprised of 26DTB-P in conjunction with a simple diol anchor and an 18-carbon tether) behaves as predicted in the aqueous and membrane compartments and retains 26DTB-P's efficacy as an inhibitor of HCN1 gating. *In vivo*, we demonstrate that BP4L-18:1:1 is an orally available antihyperalgesic with respect to mechanical allodynia and thermal hypersensitivity in an adult rat spared nerve injury (SNI) model of neuropathic pain, and shows the anticipated CNS exclusion and cardiac sparing behaviours. These data provide proof of concept that chemotypes of this form represent a novel strategy to generate therapeutics for peripheral neuropathic pain and, potentially, other clinical problems involving membrane-embedded proteins.

Methods

Molecular biology

Complementary deoxyribonucleic acids encoding murine HCN1 and, as noted, deletions thereof were subcloned into the pGH19 vector and amplified in STBL2 cells (Invitrogen, Grand Island, NY, USA). Complementary ribonucleic acid (cRNA) was transcribed from NheI linearised DNA using T7 RNA polymerase (mMessage mMachine; Ambion, Houston, TX, USA). RNA 1–50 ng was injected into each *Xenopus* oocyte.

Electrophysiology

Recordings were made from *Xenopus* oocytes 2–3 days after cRNA injection essentially as described.[25,34] Cells were maintained in a 1:1 dilution of Gibco Leibovitz's L-15 media (ThermoFisher Scientific 11415114 supplemented with 2.5% Gibco penicillin–streptomycin (10 000 U ml^{-1}; Fisher Scientific 15-140-122) and 5 mM N-(2-hydroxyethyl) piperazine-N′-2-ethane sulphonic acid (HEPES) free acid, pH 7.5 (adjusted with NaOH), at 16°C until use. Two-electrode voltage clamp (TEVC) recordings were acquired using Pulse software (HEKA Elektronik,

Lambrecht/Pfalz, Germany) and a Warner Instruments OC-725C amplifier (Hamden, CT, USA) with data digitised at 5 kHz using an ITC-18 interface (InstruTech Corp., Port Washington, NY, USA) following filtering at 2.5 kHz (902 eight-pole Bessel filter; Frequency Devices, Haverhill, MA, USA). Micro-electrodes were fabricated from 1B120F-4 borosilicate glass (World Precision Instruments, Sarasota, FL, USA) with resistances of 0.1−0.5 and 1−4 MΩ (I passing and V sensing, respectively) when filled with 3 M KCl. The Ag/AgCl ground wire(s) of the active virtual ground circuit were connected to the bath solution by 3 M KCl 2% agar salt bridges placed downstream of, but close to, the oocyte. In all cases, the observed potential was within 1% of the reported command potential. The holding potential was −30 mV, and the tail potential was 0 mV. In all recordings, the basal external solution was (in mM): 107 NaCl, 5 KCl, 1 MgCl$_2$, 1 CaCl$_2$, and 10 HEPES free acid, pH 7.4 (NaOH). All recordings were obtained at room temperature (22−24°C).

To determine the effect of alkylphenols on channel gating in TEVC, cells were placed in 20 ml glass scintillation vials (1 cell *per* vial along with 15 ml recording solution that was, where indicated, supplemented with vehicle or compound) and incubated at room temperature on a Glas-Col® tube rotator (Terre Haute, IN, USA) at slow speed. After 20 min, cells were transferred to a recording chamber continuously perfused with the appropriate drug, vehicle, or control solution. No cell was exposed to more than one condition.

Channels were activated by hyperpolarising voltage steps applied in −10 mV decrements for 3 or 5 s. The amplitude of the instantaneous tail currents after each sweep was determined as the difference between the plateau current (observed after the voltage clamp had settled and the uncompensated linear capacitance decayed but before marked channel closure) and the baseline current (observed after deactivation was complete). These relationships were then fit with a Boltzmann equation [equation (1)]:

$$I(V) = A_1 + A_2 \big/ \left\{ 1 + e^{(V - V_{1/2})/s} \right\} \qquad (1)$$

where A_1 is the current offset, A_2 is the maximal amplitude, V is the test voltage, $V_{1/2}$ is the activation midpoint, and s is the slope factor. In all cases, the parameters obtained from the short and long step paradigms were equivalent (indicating gating was equilibrated at all potentials), and the two determinations were averaged. Concentration−response data were fit using the Hill equation [equation (2)]:

$$R / R_{\max} = 1 \big/ \left\{ 1 + (IC_{50} / [A]^n \right\} \qquad (2)$$

where R is the response, $R_{\max}$ is the maximal response, $[A]$ is the alkylphenol concentration, IC_{50} is the ligand concentration that produces a half-maximal response, and n is the Hill coefficient.

To analyse gating kinetics, we fit activation time courses with a single exponential function, the origin of which was constrained by, and simultaneously determined, the lag present in each reaction. This constraint was achieved by requiring the amplitude of the exponential to equal the difference between the equilibrium level and the zero-current level after allowing uncompensated capacity currents to decay. To explore if changes in gating kinetics were strictly coupled to drug-mediated shifts in the equilibrium voltage dependence of channel gating, time constants and lags were binned with respect to the applied voltage minus

the $V_{1/2}$ for each recording. Bins were 10 mV wide, with the middle of the bin at 0 mV being equal to the $V_{1/2}$ of channel activation. Data within each step voltage minus $V_{1/2}$ bin were meaned with respect to both the value of the gating parameter and the adjusted voltage. Errors around both values are plotted.
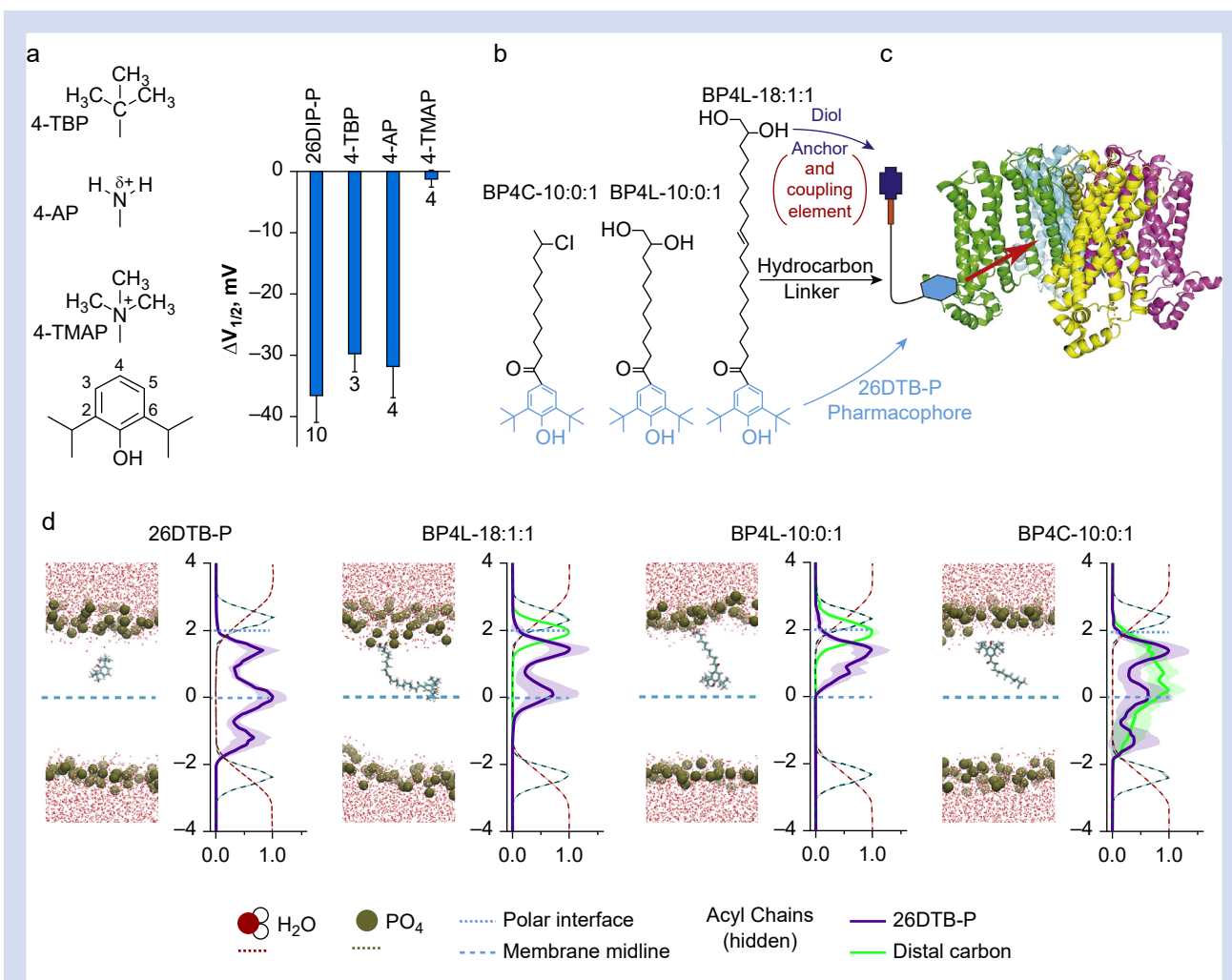
Molecular dynamics modelling

Starting configurations of the small molecules in 2-dierucoyl-*sn*-glycero-3-phosphocholine lipid bilayers were constructed using CHARMM-GUI.[38] Each simulation system contains 200 lipids (100 lipids in each leaflet) and one drug molecule. The simulation systems were hydrated, containing ~12 000 TIP3P water[39] and 0.15 M KCl. Each system was simulated for up to 300 ns in the semi-isotropic ensemble. The CHARMM36 force field was used to model the lipids.[40] The drugs were modelled with the CHARMM general force field.[41] All molecular dynamics (MD) simulations were done at 310.15 K and 1 bar using the GPU version of GROMACS (version 2018.3)[42] with a time step of 2 fs. The Nosé−Hoover thermostat[43,44] and the Parrinello−Rahman barostat[45] were used to maintain the temperature and pressure. The LINCS algorithm[46] was used to constrain water geometry and covalent bonds involving a hydrogen atom. Lennard-Jones interactions were switched off smoothly at 1−1.2 nm, and the particle mesh Ewald method[47] was used to treat long-range electrostatics with a real space cutoff distance of 1.2 nm.

Twelve simulations were run for each drug molecule (see Supplementary Videos S1−4 and Supplementary Figs S2−S5). In each case, the molecule of interest began the simulation in the aqueous compartment. It is important to note that as the simulation model is constructed using a periodic boundary condition (meaning the two aqueous phases are effectively contiguous), the model has no Z-direction polarity until the test molecule enters the bilayer. As such and in keeping with *in vitro* and *in vivo* experiments wherein the test molecule's first insertion can only be to the extracellular face of a cell membrane, in the model we define the side of first insertion to be the extracellular face and data from each simulation oriented accordingly.

Supplementary data related to this article can be found at https://doi.org/10.1016/j.bja.2023.06.067.

To independently analyse the behaviour of the pharmacophore and the distal tail of the anchor−tether complex (when present), the center of mass of the hydroxyl of the phenol and of the terminal carbon of the anchor−tether were each mapped *vs* time of the simulation, then histograms of the locations were constructed from the time of first insertion to the end of the simulation. Histograms for water and the phospholipid phosphate head groups were constructed for the entire duration of each simulation.

To generate mean behaviour across all simulations (e.g. Fig. 1), histograms were normalised and averaged, and the resultant arrays were renormalized. If a test molecule failed to insert during a simulation, the data from that run were excluded from *post hoc* processing. Whilst this approach allows us to gain insight into simulation-to-simulation variance, it weights each simulation equivalently even though runs wherein the test molecule enters the membrane late have less data compared with runs when insertion is earlier in the simulation. To address whether such weighting introduces a marked bias, we constructed cumulative histograms of the distal carbon and the phenolic raw residency data and

Fig 1. Molecular dynamic modelling demonstrates functionally tolerated *para* position anchors control within-membrane distribution of the 2,6-di-*tert*-butylphenol (26DTB-P) pharmacophore. (a) Left: structures of zero-length linker anchors used to examine the effect of charge *vs* volume on hyperpolarisation-activated cyclic nucleotide-regulated (HCN) 1 inverse agonist activity. Right: shift in the $V_{1/2}$ ($\Delta V_{1/2}$) of HCN1 gating determined in two-electrode voltage clamp (TEVC) for 2,6-di-iso-propylphenol (26DIP-P also known as propofol) and 4-substituted derivatives thereof (4-TBP, 4-*tert*-butyl-propofol; 4-AP, 4-amino-propofol; 4-TMAP, 4-trimethylamino-propofol). 26DIP-P was at 100 μM (the concentration that is saturating with respect to HCN1 inhibition); 4-TBP, 4-AP, and 4-TMAP were each at 200 μM. The effects of 26DTB-P, 4-TBP, and 4-AP are different to the absence of effect of 4-TMAP but not different to each other (see Supplementary Table S1). (b) ChemDraw representations of an unanchored (BP4C-10:0:1) and short and long tether diol-anchored variants of 26DTB-P (BP4L-10:0:1 and BP4L-18:1:1, respectively). (c) Schematic representation of the conceived coupling between a tether-anchored alkylphenol inverse agonist and an HCN1 channel. The cyan hexagon represents the alkylphenol pharmacophore. The thin black line represents the hydrophobic tether that, in the molecules presented in (b), are saturated or partially unsaturated acyl chains. The red rectangle is a hydrophilic coupling element that links the tether to the dark blue anchor. In the molecules studied here, the coupling element and the anchor are collectively the diol unit. The channel structure is adapted from Lee and MacKinnon.[48] (d) In each of the four pairs of panels, the left-hand graphic is a still image from a high-resolution molecular dynamics simulation, and the right is a normalised density distribution depicting the Z-plane occupancy within the simulation cube of the water molecules, phosphate head groups of the phospholipids, the 26DTB-P group, and the anchor–tether complex (when present) plotted with respect to the membrane midline. The behaviour of the anchor–tether complex was determined by following the distal terminal carbon (i.e., the carbon atom furthest from the pharmacophore). In each density plot, the midline of the membrane (blue dashed line) was established with respect to the distance between the phosphate peaks. Distances (in nm) are shown relative to the midline. Increasingly positive values represent the outer leaflet and extracellular medium. The location of the blue dotted line representing the polar interface was located at the maximal occupancy of the diol anchor in BP4L-18:1:1. The membrane lipid acyl chains are omitted from view for clarity.

compared each of these to their averaged normalised counterparts. The close correspondence between the cumulative and the normalised-averaged histograms indicates that the number of simulations performed and their durations are sufficient to reasonably describe the dynamic behaviour under consideration (Supplementary Fig. S6).

CNS multiparameter optimisation

CNS multiparameter optimisation (CNS MPO) scores were obtained using ClogP calculated lipid:water partition coefficient; ClogD, calculated distribution coefficient at pH 7.4; topological polar surface area; hydrogen bond donor number; molecular weight; and pKa of the most basic center calculated using Maestro within the Schrödinger Software Suite (New York, NY, USA).[49,50]

Synthesis and testing of hindered alkylphenols

See Supplementary material for details on the synthesis of hindered alkylphenols.

Reagent solubilisation

For *in vitro* electrophysiology, all butylphenol derivatives were initially solvated in dimethylsulphoxide (DMSO) then dispersed into the appropriate recording solution in either the presence or absence of a (2-hydroxypropyl)-cyclodextrin (2HPCD). Unless otherwise noted, this was 2HPβCD. BP4L-18:1:1 required the presence of 2HPCD. At the concentrations tested here, the shorter tethered molecules (BP4L-10:1:1 and BP4C-10:0:1), the zero-tether molecules (4-TBP, 4-AP, and 4-TMAP), and the parental alkylphenols (26DIP-P and 26DTB-P) could be dispersed in the presence or absence of 2HPCD. When used alone, the DMSO concentration was 0.2% v/v. When used in combination, the 2HPCD concentration was 20 mM and the DMSO concentration was 10 mM. For *in vitro* liquid chromatography with tandem mass spectrometry (LC−MS/MS) analysis, BP4L-18:1:1 was solvated in acetonitrile (ACN). For *in vivo* experiments, BP4L-18:1:1 was dissolved in peanut oil and delivered directly by gavage.

Tissue sampling and LC−MS/MS detection and quantitation

Intra-assay, 200 µl blood samples were collected by tail vein draws. Terminal collection of blood was by cardiac puncture coincident with harvesting brain, dorsal root ganglia (DRG), heart, kidney, liver, and lung. Then, 0.1 volumes of sodium citrate 10% were added to all blood samples. All samples were stored frozen at −80°C until extraction. Brain, heart, kidney, liver, and lung were each rinsed once in Dulbecco's phosphate-buffered saline, blotted dry, weighed, coarsely chopped, combined with a volume of H_2O equal to the tissue wet weight, and then homogenised using an Ultra-Turrax TP18-1051 homogeniser (Tekmar, Cincinnati, OH, USA). Blood samples and 250 µl aliquots of tissue homogenates were combined with 4 volumes of acetonitrile (ACN), vortexed, and then nutated overnight at 4°C. After warming samples to room temperature, samples were again vortexed before clarification by centrifugation for 20 min at 15,000 g at 24°C. Aliquots of each extract were diluted 1:10 by the addition of H_2O 20%:ACN 80% in low-volume glass vials and then transferred directly to the Agilent 1290 Infinity II Multisampler for immediate analysis. Whilst they were processed similarly to other solid organ samples, because of their small mass, DRG samples were combined directly with 19 wet weight volumes of H_2O and 80 volumes of ACN, processed without homogenisation, and analysed without further dilution. Inclusion of homogenisation in a low-volume loose-fitting sintered glass homogeniser did not noticeably alter extraction efficiency (not shown). In all cases, sample injection was 2 µl.

Liquid chromatography with tandem mass spectrometry was performed using an Agilent 1290 Infinity II UPLC system and an Agilent 6495 triple quadrupole mass spectrometry in positive electrospray ionisation mode. The LC column was a Phenomenex Luna C8(2) column (30 × 2 mm; 5 µm) at 30°C. The mobile phase profile was formed by a combination of solution A (formic acid 0.1% in H_2O) and solution B (formic acid 0.1% in ACN) as follows: 0−2 min 20% B linearly rising to 95% B, 2−4 min held at 95% B, 4−4.5 min 95% B linearly decreasing to 20% B, and 4.5−6 min held at 20% B. Multiple reaction monitoring was performed using the transition of m/z 517.4 → 233.1. The collision energy was 42 V with cell acceleration voltage of 2 V. The retention time of BP4L-18:1:1 was 3.93 min. Recovery and detection of BP4L-18:1:1 using this method were quantitative in all tissue types (see Supplementary Fig. S7).

Pharmacokinetic modelling

The blood concentration of BP4L-18:1:1 following a single-dose oral administration was modelled using equation (3),[51,52] where C is the blood concentration, S is the salt ionization factor, F is the fraction absorbed, D is the dose, V is the volume of distribution, k_a is the absorption rate constant, and k_e is the elimination rate constant. As BP4L-18:1:1 is not ionisable, S was set to 1:

$$C = \frac{S.F.D.k_a}{V.(k_a - k_e)} \cdot \left(e^{-k_e.t} - e^{-k_a.t} \right) \tag{3}$$

In vivo studies

All animal studies were performed using male and female rats (Sprague Dawley; age 8 weeks) following approval from the local animal care and use committee (protocol number 2010-0022) and in accordance with both institutional and federal guidelines. All behavioural and pharmacokinetic studies were performed in a triple-blind manner (behavioural studies: surgery and compound administration, person A; behavioural testing, person B; and data analysis, person C; pharmacokinetic studies: compound administration, person A; tissue processing, person B; LC−MS/MS, person C; and data analysis, person B) with compound assignment code only broken following completion of data analysis.

Neuropathic pain model

The antihyperalgesic efficacy of BP4L-18:1:1 was tested against mechanical and thermal stimuli[53] using the rat spared nerve injury (SNI)[54,55] model of neuropathic pain. The SNI model involves a lesion of two of the three terminal branches of the sciatic nerve (tibial and common peroneal nerves) whilst sparing the remaining sural nerve; this model results in robust and prolonged behavioural modifications, including mechanical and heat hyperalgesia and cold allodynia. This model is particularly advantageous to the relatively rapid and reproducible screening of compounds, as nearly all animals become neuropathic and rapidly develop both altered thermal and mechanical sensitivities.

Mechanical nociception and hyperalgesia

Exaggerated responses to mechanical stimuli were measured using von Frey filaments. We used both the traditional manual method and the electronic method. The latter has a clear advantage of eliminating subjectivity, whilst the former is the

established benchmark. Using both and demonstrating conservation of the phenotype increase qualitative confidence in the data.

Thermal and cold allodynia and hyperalgesia

Thermal hyperalgesia was measured by changes in sensitivity to changes in temperature. A Hargreaves radiant heat source was used (IITC Life Science, Woodland Hills, CA, USA) to test for heat hypersensitivity. Paw withdrawal latency was calculated between the time the desired temperature was reached and the time of withdrawal, shaking, or licking of the tested hind paw. Upon reaction of the paw, the heating of this device is rapidly reversed to standby temperatures. Cold allodynia was determined by measuring aversive behaviours caused by evaporation of a drop of acetone, which, when applied to the skin, results in a rapid (<40 s) $10-12°C$ drop in surface tissue temperature.[56] A bubble of acetone is dabbed on the plantar surface of the hind paw, and sensitivity to cold is recorded by the duration of the response (e.g. paw flicking and licking) within the first minute of application.

Efficacy testing regimen

All animals were tested, as described previously, twice before SNI surgery to establish baseline behaviour. On Day (D) 7 following induction, animals were retested for mechanical and thermal hyperalgesia and for evidence of motor impairment. By D7, all animals developed mechanical and thermal hyperalgesia, and therefore, no animals were excluded from further behavioural testing. On D28, animals were again tested for sensory and motor behaviour. Neuropathic animals were dosed with the test compound beginning D29 (described as follows), which then continued as once-daily dosing for a total of 7 days. Animals underwent repeat behavioural testing after the first and seventh doses of the test compound with tail blood samples obtained 24 h after testing.

BP4L-18:1:1 was administered *via* gavage using peanut oil as vehicle (0.5 ml). Prior data with the parent pharmacophore 26DTB-P demonstrated that a cumulative dose of 120 mg kg^{-1} (0.58 mmol kg^{-1}) was well tolerated,[25] and this was the basis for BP4L-18:1:1 dosing. Doses administered were 0.58 and 1.74 mmol kg^{-1} for sensory studies and 5.8 mmol kg^{-1} for safety studies. The rats were 8 weeks old at the time of surgery. At the end of behavioural testing, the rats were euthanised.

Motor and sedation testing

Rats were assessed using open-field and rotarod testing at 3–6 h post-drug administration. Open-field testing was performed as described.[57] Briefly, the sedative properties of BP4L-18:1:1 were tested by measuring spontaneous motor activity in an open field. Rats were tested for total distance travelled as an index of spontaneous locomotor activity in the open field at 3–6 h after administration. The Ugo Basile Rota-Rod (Stoelting Co., Wood Dale, IL, USA) was used to assess the effect of the test compound on the motor coordination of the rats. Rats were placed on textured drums to avoid slipping, and the drum was accelerated from 54 to 840 rpm. When an animal drops onto the individual sensing platforms below, the time until dropping was recorded.

Cardiovascular testing

The pan-HCN isoform inhibitor ivabradine is a negative chronotrope (i.e. it produces bradycardia without affecting contractility[58,59]). Consequently, the side-effect of most concern with an HCN inhibitor is bradycardia. To test for this, we measured HR and noninvasive BP in a separate cohort of adult rats (male and female) using a Kent CODA® noninvasive blood measuring system (Kent Scientific Corp., Torrington, CT, USA). For this, awake rats are placed in a rodent holder appropriate for their sizes, and a cuff is placed around the exposed tail. HR and BP measurements are acquired noninvasively over the span of approximately 5 min.

Abuse potential testing

We used the conditioned place preference (CPP) paradigm to determine any rewarding (or aversive) effects of the drugs.[60] In this model, an association between a specific environment and a drug treatment is formed. We used a three-compartment set-up, consisting of one black-walled compartment and a black-and-white stripe-walled compartment separated by a small connecting center compartment. Rodents are tested in three phases: habituation, conditioning, and post-conditioning (i.e. CPP test). During habituation, animals will move freely between one of two connected chambers. During conditioning, animals will be restricted to a single chamber. During this phase, the animal was dosed with the test drug and placed in one of two compartments. On the following day, the animal was administered vehicle and placed in the opposite compartment. Drug and vehicle were given on alternating days, for a total of three doses each (6 days). During the CPP test, animals again have free access to both chambers. The animal was placed in the center compartment, and the amount of time that the animal spent in each of the two test compartments (i.e. the black-walled or black-and-white striped-walled compartment) was measured. Those that have formed a preference will spend more time in the drug-paired side. This is the response expected from the morphine active comparator. Those that have not formed a preference will not show a drug-paired preference.

Statistical analysis

All data are presented as mean (standard deviation [SD]). Statistical analyses were performed in SigmaPlot V14 (Inpixon, Palo Alto, CA, USA). In all tests, a $P<0.05$ (adjusted by the relevant *post hoc* tests, as indicated) was considered significant.

Electrophysiological data were compared using either *t*-tests or one-way analysis of variance (ANOVA) with *post hoc* tests, as specified in each of the supplementary tables. For continuous behavioural data (Hargreaves; acetone), multiple groups compared by one-way ANOVA (or repeated measures ANOVA for time courses), followed by Tukey's *post hoc* testing with Bonferroni adjustment in case of multiple comparisons. For ordinal behavioural data (mechanical allodynia), data were assessed by Friedman's test with Dunn's *post hoc* test. Because of the homogeneity of the rats and the highly controlled nature of our studies and based on past experience and relevant literature, our sample size was sufficiently powered to detect an effect size of 1.3 SD at a power of 0.8. Data were analysed as a function of sex. Tissue concentrations of BP4L-18:1:1 were

compared using a *t*-test (for two populations) or a Friedman repeated measures ANOVA on ranks with Tukey test (for multiple populations). Where multiple pairwise tests were performed using ANOVA, all pairs were included in the analyses, but only those of biological significance were included in the report tables.

Results

We have shown previously that coupling between 2,6-substituted phenols (such as 26DIP-P and 26DTB-P) and HCN1 involves a hydrogen bond with the one-position hydroxyl, van der Waals interactions with the substituents on positions 2 and 6, and a dependence on ring aromaticity (see Fig. 1a for numbering).[34] Whilst these observations do not require one or more of the carbons on the undecorated back of the ring (i.e. positions 3, 4, and 5) to be lipid facing, nor do they require this face of the ring to be indifferent to the gating status of the channel, lipid exposure of one of these positions (as is seen, e.g. with 26DIP-P docked with GABA_A receptors at the general anaesthetic site[36]) is a prerequisite for the conceived anchor—tether strategy. The finding that attachment of bulky substituents to the 4-position of 26DIP-P is tolerated with respect to HCN1 inhibition if the substituent is hydrophobic (4-*tert*-butyl) or partially so (4-amino) but not if it is hydrophilic (4-trimethylamino) indicates that the 4-position (at least) satisfies the lipid exposure requirement (Fig. 1a).

To address how attachment of an extended 'anchor—tether' substituent would modify the behaviour of 2,6-substituted phenols compared with the untethered free pharmacophore, we performed a series of MD simulations comparing 26DTB-P, short (i.e. 10 carbon) and long (i.e. 18 carbon) tethered diol-anchored variants thereof (BP4L-10:0:1 and BP4L-18:1:1, respectively), and a 10:0:1 variant wherein the terminal diol of BP4L-10:0:1 is replaced with a chlorine atom (BP4C-10:0:1), thereby eliminating the hydrophilic nature of the anchor region (Fig. 1b). Figure 1c schematically shows how an ideal length anchor-tethered molecule is conceived to interact with the HCN1 channel.

Figure 1d (left pair of panels) shows a snapshot from a simulation of 26DTB-P and a plot of the residency distribution of the ligand with respect to the membrane cross section (wherein data are mean [95% confidence intervals] from 12 simulations). A representative simulation video and the individual Z-location *vs* time trajectories and Z-plane residency distributions for each simulation are available in Supplementary Video S1 and Supplementary Fig. S2.

Consistent with the inhibitory efficacy of 26DTB-P being independent of the side of presentation to the membrane (Supplementary Fig. S8), MD shows that the free alkylphenol is highly mobile in the hydrophobic phase and readily crosses the membrane midline. The distribution of free 26DTB-P is not uniform, however; despite being untethered, the molecule tends to dwell in the sub-polar regions just interior to the inner and outer leaflet hydrocarbon—phospholipid interfaces and at the juxtaposition of the acyl tails of the two leaflets. Such location preferences presumably reflect an attraction of the phenolic hydroxyl to the polar layers of the inner and outer leaflets and the lower entropic cost of displacing acyl chain tails compared with the cost of distorting the entire length of the membrane lipids, respectively.

Simulations of the tethered molecules (BP4C-10:0:1, BP4L-10:0:1, and BP4L-18:1:1) show that in the aqueous phase, the hydrocarbon tail of each molecule can exist in extended arrangements, or it can fold on itself bringing the distal tail into closer apposition with the ring (e.g. Supplementary Fig. S9). The distribution between such forms is presumably reflecting a balance between minimisation of solvent exposure of the hydrophobic elements and stiffness of the tether. Upon penetrating the head-group phase of the membrane and encountering the hydrophobic membrane core, the behaviour of the three tethered molecules is markedly divergent and is strongly controlled by the tether length and the presence or absence of a hydrophilic anchor (Fig. 1d, right-hand three pairs of panels; Supplementary Videos S2—4; Supplementary Figs S3—S6).

A close inspection of the time trajectories of BP4L-18:1:1 and BP4L-10:0:1 shows that whilst the order of first insertion into the phosphate head-group layer is random (in different simulations, insertion can commence with either the diol or the phenolic group; data not shown), it is always the 26DTB-P moiety that descends into the hydrophobic core. The residency distributions confirm this post-insertion configuration. Indeed, an inspection of the distributions of the terminal carbon of the anchor—tether complexes of both BP4L-18:1:1 and BP4L-10:0:1 (Fig. 1d; Supplementary Figs S3 and S4) shows that post-insertion, the diol anchor is almost exclusively retained at the inner face of the extracellular polar head-group layer, and its distribution in that location is essentially Gaussian. In contrast, the phenolic groups of both BP4L-18:1:1 and BP4L-10:0:1 tend to locate deeper in the membrane, where both show a bimodal distribution.

In the background of the long tether present in BP4L-18:1:1, the preferred locations of the 26DTB-P moiety are the outer leaflet sub-polar region and at the membrane midline. These locations exactly mirror two of the three locations preferred by free 26DTB-P. Whilst also bimodal, the phenolic group of BP4L-10:0:1 does not reach as far into the membrane, and its deeper location is at an intermediate depth, a location that is disfavoured by free 26DTB-P. In striking contrast to free 26DTB-P, there is no significant occupancy of the inner leaflet sub-polar region by the 26DTB-P head group of either BP4L molecule. This finding reveals that the tethered pharmacophore makes few deeper sojourns into the membrane, and there is no tendency for the diol to 'flip' to the intracellular face and equalise the drug distribution between the two leaflets.

The dominant role of the diol anchor in controlling the behaviour of the BP4L molecules is revealed by comparison with the residency distribution of the anchorless molecule BP4C-10:0:1 (Fig. 1d; Supplementary Fig. S5). First, the distal carbon in BP4C-10:0:1 shows a broad location distribution across the entire width of the inner leaflet. Second, and consistent with the lack of anchoring by the Cl substitution, the phenolic group of BP4C-10:0:1 shows a distribution that is essentially indistinguishable to free 26DTB-P, including occupancy of the inner leaflet sub-polar region.

As MD simulations are computationally expensive, limiting them to molecular (nanoseconds to microseconds) and not biological timescales (milliseconds to minutes), we cannot directly address the fate of the molecules at longer times. However, given the low rate of uncatalysed flipping of lipids,[63] unless it is the substrate of a flippase, a molecule, such as BP4L-18:1:1, would be expected to stay stably inserted in the outer leaflet.

The length of an individual carbon—carbon single bond is ~1.4 Å. Given its 'kinked' nature, the length of an extended acyl

chain ordinate to the membrane is ~1 Å per bond. On this basis, the longest reach of the phenolic groups of BP4L-10:0:1 and BP4L-18:1:1 would be expected to be ~10 and ~18 Å, respectively. As can be seen in the residency distributions, the mean furthest reach of the head groups relative to their diols were observed to be ~13 and ~19 Å, respectively.

The largely unsaturated nature of the acyl tethers of BP4L-18:1:1 and BP4L-10:0:1 was intended to permit the molecule to have sufficient flexibility to maximise the likelihood that the pharmacophore could orient productively with respect to the inhibitory site on HCN1; this flexibility is readily apparent in the MD video files (as per representative Supplementary Videos S1–4). Significant occupancy of the outer leaflet sub-polar region by the 26DTB-P head group of both BP4L-10:0:1 and BP4L-18:1:1, in addition to occupancy of their deepest-reach sites, demonstrates that the anticipated design feature of flexibility is satisfied.

These data show that a diol anchor-tethered ligand functions as conceived with respect to the membrane, and they make simple predictions with respect to the anticipated inhibitory efficacy and potency of this family of molecules. Specifically, if the HCN1 inhibitory site is in the sub-polar region, all the ligands should be similarly effective as channel inhibitors, whereas if the HCN1 inhibitory site on HCN1 is in the mid-membrane region, the inhibitory potency of this family of molecules should conform to BP4L-18:1:1 ≥ 26DTB-P > BP4C-10:1:1 > BP4L-10:1:1. To examine this directly, we generated all three tethered molecules: BP4C-10:0:1, BP4L-10:0:1, and BP4L-18:1:1.

For ease of synthesis, we used an acylation strategy (see Methods). Whilst this involved the incorporation of a ketone adjacent to the ring, which increased the local volume, the data reported in Figure 1a suggest this would not in or of itself cause a steric clash with the channel.

Figure 2a shows representative HCN1 channel-generated currents recorded from *Xenopus* oocytes using TEVC in the absence or presence of 30 μM BP4L-18:1:1 and superimposed fits of a constrained single exponential function that simultaneously determines the pre-exponential lag and the exponential time constant. Figure 2b shows tail current activation curves from a series of cells from the same donor frog exposed to varying concentrations of BP4L-18:1:1. Figure 2c and d plots the time constant of activation kinetics (Fig. 2c) and the inverse of the time constant (which, at limiting potentials, gives an approximation of the voltage-independent opening rate[64]; Fig. 2d), each as a function of the imposed activation step potential relative to the observed $V_{1/2}$. Figure 2e plots the shift in HCN1 channel gating as a function of BP4L-18:1:1 concentration. An inspection reveals that BP4L-18:1:1 elicits profound left-shift in, and slowing of, gating. Whilst these findings closely mirror the impairment of channel opening seen with unhindered alkylphenols,[25,34] a notable difference between inhibition by BP4L-18:1:1 and unhindered alkylphenols is that where channel slowing by the latter class of molecules involves a simple translation of kinetics along the voltage axis as a function of the shift in the equilibrium gating term ($V_{1/2}$), inhibition by BP4L-18:1:1 additionally causes an approximately four-fold slowing of the limiting opening rate (Fig. 2c and d). We attribute this to the acyl tether of the hindered alkylphenol packing along the length of the targeting groove between the voltage-sensing paddles adding to the work the pore needs to do to transit to its open configuration. Nonetheless, the general similarity in potency and maximal efficacy of inhibition by BP4L-18:1:1

and 26DTB-P is consistent with them acting in a conserved manner against a common site.

Finally, we asked if *in vitro* studies could shed light on the efficacy of the diol anchor. Figure 2f compares the tail current activation curves of HCN1 in the presence of vehicle, BP4L-10:0:1, and BP4C-10:0:1. Both BP4C-10:0:1 and the similarly unanchored synthesis intermediate, BP4K-10:0:1 (data not shown), were effective inverse agonists of HCN1, whereas BP4L-10:0:1 was not. In tandem with our MD simulation studies, the conservative interpretation is that even a simple anchor, such as a diol, is adequate to control membrane (and potentially BBB) penetration with the tether of BP4L-10:0:1 being too short to permit the 26DTB-P pharmacophore to reliably reach its binding site on the channel.

To examine acute and cumulative bioavailability, we delivered BP4L-18:1:1 at either 0.58 or 1.74 mmol kg^{-1} *via* gavage. Figure 3a shows the time course of BP4L-18:1:1 in the blood of adult rats over a 30 h period following administration of a single dose. Based on the broad peak in the blood concentration, all behaviour experiments were performed in the 3–6 h window following gavage on the day of behavioural testing. Parameter estimates based on fits of equation (3) (see Methods) to the blood time courses are shown in Figure 3b. Figure 3c shows the concentration in rat blood 6 h after a single enteral dose and 6 h after the seventh such once-daily bolus. Together, these data show that BP4L-18:1:1 is rapidly and readily absorbed from the gut; that there is an initial dose dependence to the blood load; and that, whilst there may be a modest sex-dependent difference in the pharmacokinetics (that can be best modelled as a modestly higher clearance rate in females *vs* males), following 7 days of dosing this difference is inconsequential, and the blood loads detected in females and males overlap.

Most drugs cross the BBB by transmembrane diffusion; a low molecular weight and high degree of lipid solubility favour crossing by this non-saturable mechanism.[65] The strongly validated and widely used CNS MPO algorithm predicts that molecules with a score of 4 or below will be effectively excluded from the CNS.[49,50] The CNS MPO score for BP4L-18:1:1 is 2.25, indicating that it should have little, if any, entry into the CNS. To examine this directly, we harvested tissues from the animals shown in Figure 3b at the time of the terminal blood draw 6 h after the seventh daily bolus. Figure 4 shows the tissue load for each animal normalised to the individual's blood concentration at the time of tissue harvest. The liver and heart appear to be in effective equilibrium with the blood (mean liver:blood ratio 1.67; heart:blood ratio 0.76). In contrast, the data in Figure 4 demonstrate that BP4L-18:1:1 is, as predicted, poorly, if at all, penetrant to the brain (mean brain:blood ratio 0.007). Importantly, whilst the DRG:blood ratio is lower than is seen with the lung and kidney (0.04, 0.19, and 0.14, respectively), it trends higher than brain. Moreover, it is important to note that the DRG samples were primarily the ganglia themselves (which are partially protected by the BBB) and not the distal nerve projections of the nerves that are outside the BBB and where HCN1 inhibition is likely to contribute to overall therapeutic efficacy.[66–68]

We next asked whether the hindered molecule is antihyperalgesic, and this was tested using the rat SNI model of neuropathic pain.[54] Mechanical hyperalgesia can be measured using either manual von Frey filaments or an automated (electronic) system. Whilst the former is the established benchmark and the latter has the advantage of eliminating subjectivity,[53] as the two methods can give
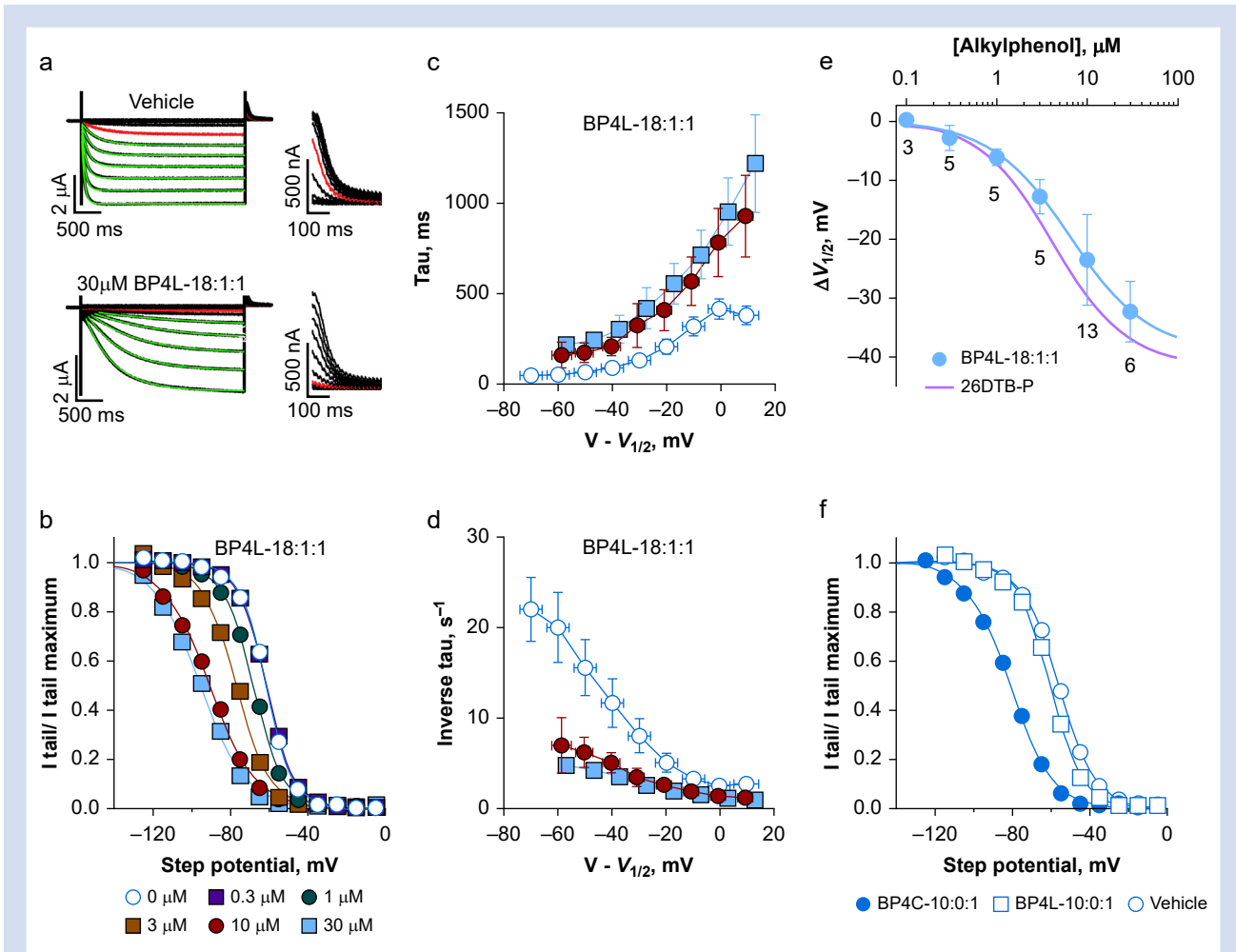
Fig 2. BP4L-18:1:1 is a potent and efficacious hyperpolarisation-activated cyclic nucleotide-regulated (HCN) 1 inverse agonist. (a) Exemplar families of HCN1 two-electrode voltage clamp (TEVC) current traces (left, full length; right, the tail currents on expanded scales). Current traces in red were those obtained upon activation at −65 mV. The green lines are superimposed fits of a single exponential function that simultaneously optimises the time constant and the pre-exponential lag. Human HCN1 was similarly inhibited by BP4L-18:1:1 (data not shown). (b) Representative normalised tail current activation curves, each fits with the Boltzmann function. Each curve is from a different cell, but all are from the same donor frog recorded on the same day. (c, d) Activation time constants (c) and their inverse (d), plotted as a function of the step potential with respect to the $V_{1/2}$ with data aggregated into 10 mV bins. Errors around the dependent variables and around the binned $V-V_{1/2}$ are standard deviation (SD). Where no error is seen, it is smaller than the symbol. Data are from nine, six, and six separate recordings (control, 10 μM, and 30 μM, respectively) paired by day and donor frog. (e) Shift in the $V_{1/2}$ of HCN1 gating, as determined in TEVC in the presence of BP4L-18:1:1 (filled blue circle, blue line is the superimposed fit of the Hill equation). Data are mean [SD]; the number of cells are indicated below each symbol. The potency and efficacy of HCN1 inhibition by BP4L-18:1:1 (IC$_{50}$=6.4 μM; $\Delta V_{1/2\ MAX}$=−38.9 mV; Hill coefficient=1.0) is comparable with that by free 2,6-di-*tert*-butylphenol (26DTB-P) (IC$_{50}$=4.2 μM; $\Delta V_{1/2\ MAX}$=−41.3 mV; Hill coefficient=1.1; the red line is the Hill fit to the shift in the $V_{1/2}$ of HCN1 gating in response to 26DTB-P (see Supplementary Fig. S9). $\Delta V_{1/2}$ in 3, 10, and 30 μM BP4L-18:1:1 (but not 1, 0.3, or 0.1) are significantly different from vehicle controls (Supplementary Table S2) but are not different from the respective $\Delta V_{1/2}$ in 3, 10, and 30 μM 26DTB-P (Supplementary Table S3). (f) Representative current−voltage relationships for HCN1 I_h currents in the absence and presence of 100 μM BP4L-10:0:1 (short diol-anchored molecule) or BP4C-10:0:1 (the equally short but unanchored chlorine variant) indicate BP4L-10:0:1 is less effective than BP4C-10:0:1 (mean $\Delta V_{1/2}$ values [SD] were −3.6 [5.5], n=5 and −24 [6.3], n=5; −21.3 [2.4], n=5, respectively) and either the longer diol-anchored molecule, BP4L-18:1:1 (a−e) or the unanchored synthesis intermediate, BP4K-10:0:1 (mean $\Delta V_{1/2}$ [SD], −21.3 [2.4], n=5 at 30 μM; not shown). The $\Delta V_{1/2}$ values in BP4C-10:0:1 and BP4K-10:0:1 are significantly different from BP4L-10:0:1 but not from each other (Supplementary Table S4).

discordant results depending on the nerve injury model used,[69] we elected to take the conservative approach and use both.

Baseline measurements in separate cohorts of male and female rats were obtained 7 and 3 days before surgery to establish reference thresholds, following which animals underwent nerve ligation or sham surgery (D0). Animals were retested 7 (D7) and 28 (D28) days after surgery. As reported in Figure 5a and b, in nerve ligation animals, mechanical hyperalgesia was clearly present on D7 and was stable over time. With single-dose administration of BP4L-18:1:1 (*via* gavage), there was a significant dose-dependent improvement in
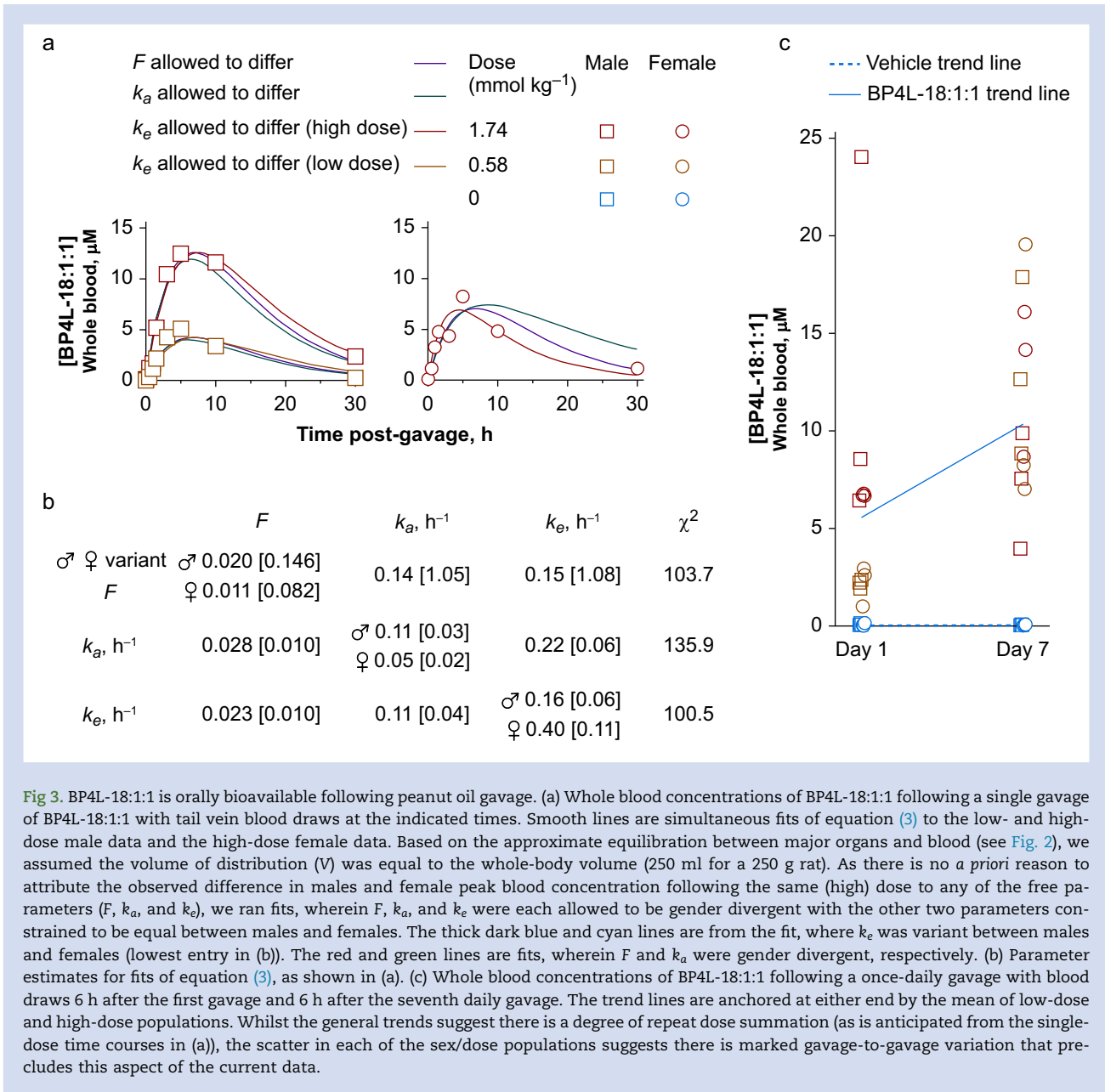
Fig 3. BP4L-18:1:1 is orally bioavailable following peanut oil gavage. (a) Whole blood concentrations of BP4L-18:1:1 following a single gavage of BP4L-18:1:1 with tail vein blood draws at the indicated times. Smooth lines are simultaneous fits of equation (3) to the low- and high-dose male data and the high-dose female data. Based on the approximate equilibration between major organs and blood (see Fig. 2), we assumed the volume of distribution (V) was equal to the whole-body volume (250 ml for a 250 g rat). As there is no *a priori* reason to attribute the observed difference in males and female peak blood concentration following the same (high) dose to any of the free parameters (F, k_a, and k_e), we ran fits, wherein F, k_a, and k_e were each allowed to be gender divergent with the other two parameters constrained to be equal between males and females. The thick dark blue and cyan lines are from the fit, where k_e was variant between males and females (lowest entry in (b)). The red and green lines are fits, wherein F and k_a were gender divergent, respectively. (b) Parameter estimates for fits of equation (3), as shown in (a). (c) Whole blood concentrations of BP4L-18:1:1 following a once-daily gavage with blood draws 6 h after the first gavage and 6 h after the seventh daily gavage. The trend lines are anchored at either end by the mean of low-dose and high-dose populations. Whilst the general trends suggest there is a degree of repeat dose summation (as is anticipated from the single-dose time courses in (a)), the scatter in each of the sex/dose populations suggests there is marked gavage-to-gavage variation that precludes this aspect of the current data.

mechanical hyperalgesia, and the observed antihyperalgesic effect was enhanced when tested at 7 days following daily dosing. Importantly, the findings reported by both the electronic and manual methods are qualitatively identical. As shown in Supplementary Figure S10, sham animals displayed no hyperalgesia and no BP4L-18:1:1-altered response to mechanical stimuli. Statistical comparisons are reported in Supplementary Table S11.

With 1 day treatment, the antihyperalgesic efficacy of low-dose BP4L-18:1:1 (0.58 mmol kg⁻¹) in male rats was not different from the high dose (1.78 mmol kg⁻¹) when measured electronically (P=0.1645), but it was different when measured manually (P=0.0003). With 7 days of dosing, the high-dose male group showed a significant improvement over the low-dose male group regardless of how the response was measured (electronic, P=0.0244; manual, P<0.0001). In female

rats, the antihyperalgesic efficacy of high-dose BP4L-18:1:1 against mechanical hyperalgesia was significantly greater than that of the low dose on D1 (electronic, P=0.0037; manual, P=0.0221) but not with 7 days of drug administration (electronic, P=0.6001; manual, P=0.0962). In both males and females, low and high drug dosing was always superior to vehicle (peanut oil).

Figure 5c and d reports the effect of BP4L-18:1:1 on thermal allodynia. To test for cold allodynia, the acetone test was used (Fig. 5c).[56] In both male and female rats, high- but not low-dose BP4L-18:1:1 was anti-allodynic with 1 day of drug administration (compared with vehicle). With 7 days of dosing, both high and low doses provided significant relief (compared with vehicle), and the high dose provided significantly more relief than the low dose (males, P<0.0001; females, P=0.0071; Supplementary Table S11, bottom). Allodynia to heat was
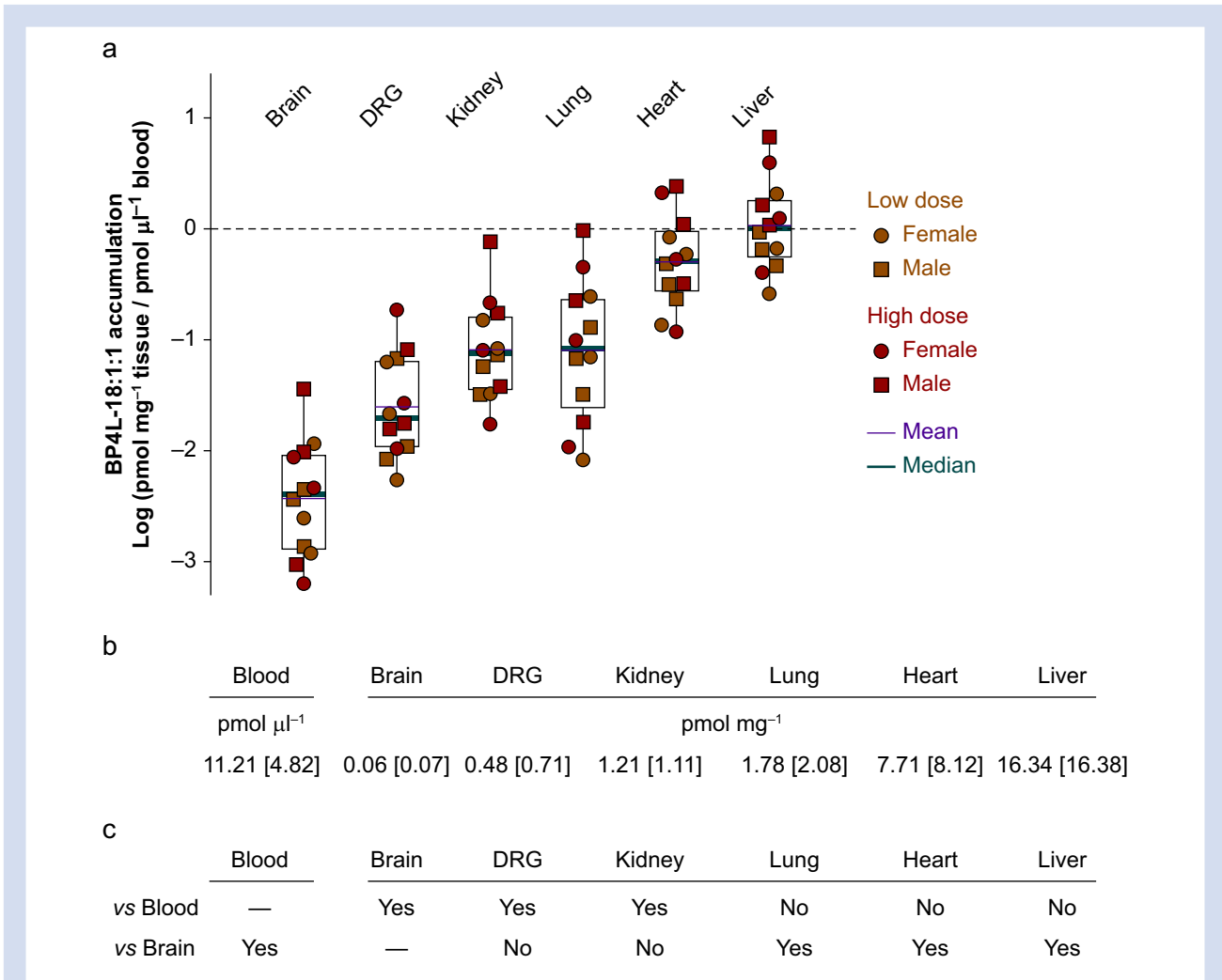
Fig 4. BP4L-18:1:1 is excluded from the CNS and shows variable access to peripheral tissues. (a, b) Following once-daily dosing by gavage for 7 days, blood and tissue samples were taken from 12 randomly selected animals (three animals from each of the four plus-BP4L-18:1:1 behavioural cohorts reported in Fig. 5). The box plots in (a) report the BP4L-18:1:1 accumulation in each tissue relative to the blood concentration in the same animal. Note that tissue loads of pmol mg^{-1} wet weight are equivalent to µM, assuming the tissue density is 1[61,62] and the drug can distribute freely across the entirety of the tissue. Based on the overlap in the ratios of the high and low dose and male and female populations (as per (a)) and a lack of difference between the tissue loads of male vs female ($P=0.464$) and high dose vs low dose ($P=0.430$) (as per Student's t-test comparisons), (b) reports the mean tissue loads [standard deviation] across the combined samples (males plus females at both high and low doses). (c) A Friedman repeated measures analysis of variance on the tissue loads indicates brain, dorsal root ganglia (DRG), and kidney are protected organs relative to blood, whereas lung, heart, and liver are in near equilibrium with blood. For full statistical comparisons, see Supplementary Table S5.

assessed using the Hargreaves method.[70] In the SNI model, sensitivity to heat is detectable, although the hypersensitivity is less pronounced than that for cold,[54,71] and the observed hypersensitivity following nerve injury reported here is consistent with prior observations. In male rats, both low- and high-dose BP4L-18:1:1 relieve heat sensitivity at the end of 7 days of dosing with the same degree of efficacy (Fig. 5d, left; Supplementary Table S11, bottom). In female rats, only the high dose was anti-allodynic (Fig. 5d, right; Supplementary Table S11, bottom).

The HCN channels are highly expressed throughout the heart, and non-selective HCN block with ivabradine results in sinus bradycardia.[72] Although HCN4 is the most predominant isoform with notable expression of HCN2, species variation[29,73–76] leaves open the possibility that an HCN1 antagonist might also have bradycardic properties. We tested BP4L-18:1:1 at 1.74 mmol kg^{-1} (data not shown) and 5.8 mmol kg^{-1} (respectively, three and 10 times the lowest dose examined with respect to antihyperalgesia), and even after a 7 day dosing regimen, there was no change in either HR or BP (Fig. 6a).

As with humans (see Supplementary Fig. S1), HCN1 channels are widely distributed throughout the rat brain.[77] Despite the low CNS penetration, to test for CNS side-effects, we also examined the effects of high-dose BP4L-18:1:1 (5.8 mmol kg^{-1}) on motor coordination and sedation using rotarod and open-field tests, respectively. At a dose that is 10 times a
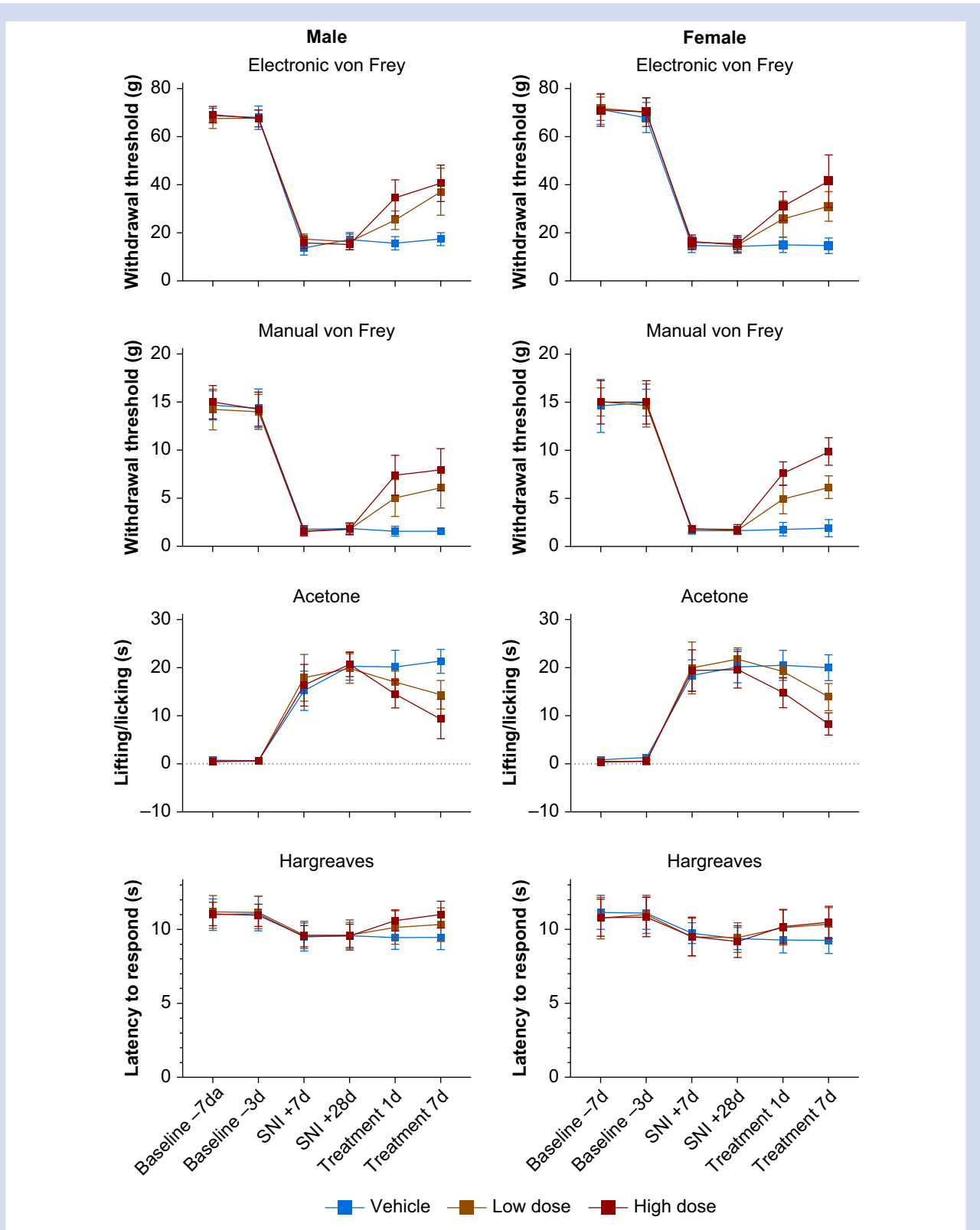
Fig 5. BP4L-18:1:1 relieves sciatic spared nerve injury-induced mechanical allodynia and thermal hyperalgesia in a dose-dependent manner in male and female rats. The top four panels examine mechanical allodynia by plotting the withdrawal threshold of the paw ipsilateral to SNI injury in response to mechanical stimuli applied using (a) electronic and (b) manual von Frey procedures. Hypersensitivity to (c) cold and (d) hot thermal stimuli were determined by observing the length of time an animal lifted/licked the injured/tested paw (cold) and the latency before the animal withdrew its foot from the heat source (hot). In all panels, the timing of baseline and post-surgical measurements is in days ('d') with respect to the day of surgery (as detailed below (d)). Treatment is 1 or 7 days of once-daily dosing with vehicle or the indicated dose of BP4L-18:1:1 with timing relative to the SNI+28d determination. Thirty-six animals were used in total, with 12 animals each randomly assigned to vehicle, low-dose, and high-dose groups. Low dose, 0.58 mmol kg^{-1}; high dose, 1.74 mmol kg^{-1}. Data are presented as mean [standard deviation].
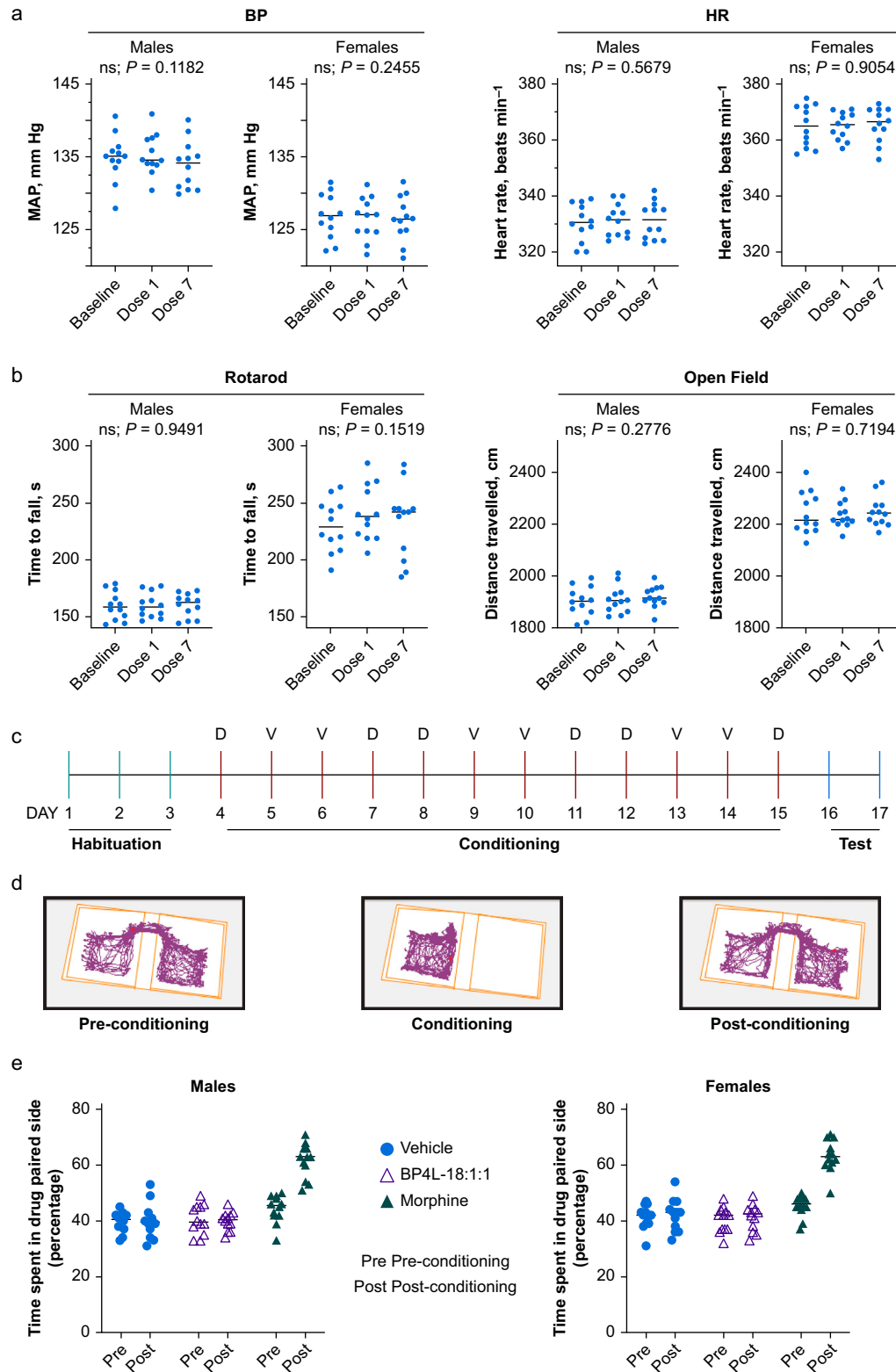
Fig 6. BP4L-18:1:1 is devoid of adverse effects on cardiovascular function and motor activity and lacks abuse potential. (a) Cardiovascular measurements were taken 1 h after dosing. Twenty-four animals total (12 males; 12 females). Data for each animal are from 20 individual HR and BP (MAP) measurements. Doses 1 and 7 indicate the total number of days dosed. Statistics: repeated measures analysis of variance. (b) Motor measurements were taken 1 h after dosing. Twenty-four animals total (12 males; 12 females). Data for each animal are from 10 replicates using the Ugo Basile Rota-Rod ramping from 5 to 80 rpm. Motor activity was measured using the Stoelting ANY-box automated tracking system. Total activity was measured over 20 min. (c) Schematic representation of the conditioned place paradigm training and dosing schedule (D, drug; V, vehicle). (d) An example of a preference trail map for a single rat. (e) BP4L-18:1:1 (5.8 mmol kg^{-1}) did not lead to place preference in either male (left panel) or female (right panel) rats. In contrast, morphine (5 mg kg^{-1}, s.c.) produced a robust place preference ($P<0.0001$ vs vehicle and BP4L-18:1:1, and $P<0.0001$ for morphine pre- and post-conditioning).

significantly effective antihyperalgesic dose (i.e. 0.58 mmol kg^{-1}) in both male and female rats, there was no effect on either motor coordination or activity levels after 1 or 7 days of once-daily dosing (Fig. 6b).

The prototypical clinically used alkylphenol general anaesthetic, 26DIP-P (also known as propofol), does not modulate G-protein-coupled inwardly rectifying potassium channels,[78] including those linked to μ-opioid receptors,[79] suggesting that alkylphenol-based ligands, such as BP4L-18:1:1, would be unlikely to have abuse potential comparable with opioid-based analgesics. This was explicitly tested using a CPP paradigm. As shown in Figure 6c–e, BP4L-18:1:1, at 5.8 mmol kg^{-1}, a dose that is 10 times a significantly effective antihyperalgesic dose (i.e. 0.58 mmol kg^{-1}) does not lead to place preference in either male or female rats. The absence of an effect with BP4L-18:1:1 contrasts with the positive control, morphine sulphate (5 mg kg^{-1}, s.c.), which produces a robust place preference in both male and female rats.

Discussion

Extensive preclinical studies have suggested that HCN channels contribute to the development of peripheral neuropathic pain,[21,22] and gene deletion studies have clearly linked HCN1[80] and HCN2[27,81] to aspects of this disorder. Importantly, and in contrast to previous data obtained from normal healthy human subjects,[82] in patients with clearly diagnosed chronic peripheral neuropathic pain, the nonspecific HCN pore blocker ivabradine was observed (in a mixed-linear model) to relieve neuropathic pain in a dose-dependent fashion, providing first-in-human evidence of HCN channel engagement in peripheral neuropathic pain.[83]

To exploit these insights therapeutically, it is necessary to address three questions. Firstly, which isoform(s) predominate in human DRG? Secondly, can a therapeutic strategy be designed to mitigate potential unwanted side-effects because of the widespread HCN channel expression and the diverse functional roles of pacemaker channels? Thirdly, can a therapeutic strategy be designed that addresses or exploits channel diversity that arises from subunit co-assembly?

In rodents, HCN2 and HCN1 appear to dominate in DRG neurones. Thus, whilst the number of DRG neurones expressing HCN2 is essentially identical to the number expressing HCN1, 71.5% and 70.9%, respectively),[84] HCN2 mRNA expression levels are greater than that for HCN1 regardless of cell size or animal age.[85] Importantly, in human DRG neurones, HCN1 mRNA is present in a larger proportion of neurones than is HCN2 (94.4% *vs* 44.0%, respectively),[84] and HCN1 may be more robustly expressed than HCN2, where the RNA expression is, in transcripts per million (median [25%; 75%]): HCN1 (63.2 [55.3; 80.9]) and HCN2 (30.7 [23.5; 50]).[86] As such, human sensory neurone I_h is likely to be largely formed from HCN1 homotetramers and heterotetramers comprised of HCN2 and HCN1. A dominant role for HCN1 in human DRG is further suggested by functional expression. Thus, whole-cell patch clamp recordings from human pluripotent stem cell-derived sensory neurones reveal the presence of cAMP-insensitive I_h currents with fast activation kinetics,[87] consistent with the expression of HCN1 homotetramers and possibly HCN1–HCN2 heterotetramers.[32] In contrast to the robust, if divergent, expression of HCN1 and 2, HCN3 and 4 have low transcript numbers in human DRG (median [25%; 75%]: 5.8 [4.6;

7.7] and 2.2 [1.4; 2.8], respectively),[86] suggesting they are of limited functional importance therein, a finding that accords with neither HCN3[88] nor HCN4[85,89,90] appearing to contribute significantly to peripheral neuropathy in rodents.

Hyperpolarisation-activated cyclic nucleotide-regulated channels are present in cardiac tissues and are thought to play a key function in the generation of intrinsic oscillatory electrical activity ('pacemaking') in the heart.[91] As is observed with DRG neurones, there are notable differences in expression between species. HCN2 protein expression is readily observed in human atrial and ventricular tissues,[29,30] along with HCN2 mRNA in sinoatrial and paranodal areas.[31] In contrast, HCN1 protein is absent from both human atrial and ventricular heart tissue obtained from patients with normal and ischaemic myopathic hearts.[29] In sinoatrial node (SAN) pacemaker cells, HCN1 mRNA is present[31,92] but at a much lower level (approximately seven-fold) than HCN4,[31] and the same appears to be the case along the atrioventricular conduction axis.[93] Consistent with the proposition that HCN4, and not HCN1, is primarily responsible for SAN pacing in the human heart is the observation that cardiac arrhythmias associated with the cardiac pacemaker current I_f (which is equivalent to the neuronal I_h current) are limited to mutations in HCN4[94] (for review, see Verkerk and Wilders[95]). Accordingly, it seems likely that selectively targeting HCN1 will minimise unacceptable cardiac effects, whereas targeting HCN2 (an approach that has received significant pharmaceutical interest[96]) carries a marked risk.[97] As all four HCN isoforms are widely distributed within the CNS (see Supplementary Fig. S1), central exclusion is likely to be a critical feature of any peripherally acting HCN antagonist.

Consideration of ivabradine highlights the concerns raised with regard to using HCN antagonists against isoforms other than HCN1, especially those that are also CNS penetrant, for peripheral antihyperalgesia. Ivabradine is a bradycardic agent[98,99] that, following early reports demonstrating improved survival in patients with coronary artery disease and poor left ventricular function,[100,101] was approved worldwide for this indication.[102,103] Consequently, bradycardia will be an unavoidable and undesirable side-effect of nonselective HCN inhibition with drugs, such as ivabradine.[83] Moreover, and despite claims to the contrary, ivabradine crosses the BBB, as indicated by changes in seizure threshold in multiple rodent models,[104–109] even when administered systemically,[109] which may result in unwanted CNS side-effects over the long term. Together, the aforementioned observations suggest that HCN1 is the preferable primary target for peripheral antihyperalgesia, and a strategy that will inhibit both homomeric HCN1 channels and heteromers incorporating HCN1 will be the optimal approach.

Based on evidence that HCN1-selective[33,34,110] gating modifiers of the alkylphenol family can inhibit HCN1-containing heterotetramers,[33] we hypothesised that a 'hindered' version of such an inhibitor would retain its efficacy as both an HCN1 inhibitor and as an antihyperalgesic but could be prevented from crossing in the CNS. Here, we use *in silico*, *in vitro*, and *in vivo* approaches to evaluate this hypothesis. Exploiting the membrane-mediated access of alkylphenols to their inhibitory site on HCN1,[34] we designed a novel class of molecules comprising the alkylphenol pharmacophore coupled to a hydrophilic 'anchor' by way of a hydrophobic 'tether'.

In silico and *in vitro* studies provide a robust proof of principle for the anchor-tethering strategy *per se* by showing outer leaflet retention of the molecule with respect to a cell membrane and by showing BP4L-18:1:1 (a variant with an 18-carbon tether between the pharmacophore and the diol anchor) retains the 26DTB-P pharmacophore efficacy as an HCN1 channel inverse agonist. Importantly, *in silico* and *in vivo* data confirm that our 'anchor–tether' strategy effectively prevents BP4L-18:1:1 from crossing the BBB. Critically, we further show that BP4L-18:1:1 retains the antihyperalgesic efficacy of the free 26DTB-P pharmacophore with respect to relief of both mechanical hyperalgesia and thermal allodynia, and it does so without either cardiovascular or central side-effects.

As noted earlier, other HCN1-selective inhibitors have been described but with markedly different structures from BP4L-18:1:1.[23,24,111] Like BP4L-18:1:1, these molecules are also antihyperalgesic in nerve injury[24] and chemotherapy-induced[26] neuropathic pain models. A notable advantage to the use of the alkylphenol 26DTB-P as the pharmacophore is the observation that the congener 2,6-di-*iso*-propylphenol inhibits HCN1 homotetramers and HCN1–HCN2 heterotetramers with equal efficacy,[33] but it has little or no effect on HCN2 homotetramers.[33,34,110] This is relevant, as HCN1 and HCN2 will freely co-assemble to form functional heterotetramers when heterologously expressed,[32] and this appears to be also true in hippocampal[112,113] and DRG neurones.[114] As there is an apparent common binding site for 2,6-di-substituted alkylphenols,[34] an antihyperalgesic that incorporates 26DTB-P should work equally well as an inverse agonist for HCN1 homotetramers and HCN1–HCN2 heterotetramers because of the incorporation of HCN1.

In summary, we have validated the hindered anchor–tether strategy, which we designed to selectively target a membrane-embedded protein (HCN1) expressed in peripheral neurones. This approach is entirely concordant with the assessment that targeting sensory neurone hyper-excitability constitutes an approach to developing new drugs for the treatment of neuropathic pain and the recommendation that 'novel drugs that target peripheral sites must have minimal access to the CNS even when administered systemically and should not interfere with normal protective sensations'.[115] Moreover, in so doing, we have generated proof of principle for a novel therapeutic chemotype that can be expanded to target any number of membrane proteins in the periphery for which lipophilic modifiers of function exist.

Authors' contributions

Project conception: GRT, PAG
Experimental design: GRT, RU, JDW, NPB, RLJ, MAF, WM, VSCW, DCG, MWC, CJC, ZL, GZ, NED, DNB, DS, HII, AAS, DEW
Data collection/analysis: GRT, RU, JDW, NPB, RLJ, MAF, WM, VSCW, DCG, MWC, CJC, ZL, GZ, NED, DNB, DS, HII, DEW
Writing of the manuscript: GRT, PAG
Editing of the manuscript: GRT, JDW, DEW, PAG

Declarations of interest

GRT, PAG, AAS, RU, JDW, RLJ, and DNB are co-inventors on patents related to the development of novel alkylphenols for the treatment of neuropathic pain. PAG, GRT, DEW, and JDW serve on the Scientific Advisory Board for Akelos (New York, NY, USA), a research-based biotechnology company that has secured a licensing agreement for the use of those patents.

Appendix A. Supplementary data

Supplementary data to this article can be found online at https://doi.org/10.1016/j.bja.2023.06.067.

References

1. Gaskin DJ, Richard P. The economic costs of pain in the United States. *J Pain* 2012; **13**: 715–24
2. Breivik H, Eisenberg E, O'Brien T, OPENMinds. The individual and societal burden of chronic pain in Europe: the case for strategic prioritisation and action to improve knowledge and availability of appropriate care. *BMC Public Health* 2013; **13**: 1229
3. von Hehn CA, Baron R, Woolf CJ. Deconstructing the neuropathic pain phenotype to reveal neural mechanisms. *Neuron* 2012; **73**: 638–52
4. Freynhagen R, Bennett MI. Diagnosis and management of neuropathic pain. *BMJ* 2009; **339**: b3002
5. Finnerup NB, Attal N, Haroutounian S, et al. Pharmacotherapy for neuropathic pain in adults: a systematic review and meta-analysis. *Lancet Neurol* 2015; **14**: 162–73
6. Colloca L, Ludman T, Bouhassira D, et al. Neuropathic pain. *Nat Rev Dis Primers* 2017; **3**, 17002
7. Smith EM, Pang H, Cirrincione C, et al. Effect of duloxetine on pain, function, and quality of life among patients with chemotherapy-induced painful peripheral neuropathy: a randomized clinical trial. *JAMA* 2013; **309**: 1359–67
8. Rao RD, Michalak JC, Sloan JA, et al. Efficacy of gabapentin in the management of chemotherapy-induced peripheral neuropathy: a phase 3 randomized, double-blind, placebo-controlled, crossover trial (N00C3). *Cancer* 2007; **110**: 2110–8
9. Jensen TS, Madsen CS, Finnerup NB. Pharmacology and treatment of neuropathic pains. *Curr Opin Neurol* 2009; **22**: 467–74
10. Dray A. Neuropathic pain: emerging treatments. *Br J Anaesth* 2008; **101**: 48–58

11. Busse JW, Wang L, Kamaleldin M, et al. Opioids for chronic noncancer pain: a systematic review and meta-analysis. *JAMA* 2018; **320**: 2448–60

12. McNicol ED, Ferguson MC, Schumann R. Methadone for neuropathic pain in adults. *Cochrane Database Syst Rev* 2017; **5**: CD012499

13. Cooper TE, Chen J, Wiffen PJ, et al. Morphine for chronic neuropathic pain in adults. *Cochrane Database Syst Rev* 2017; **5**: CD011669

14. Derry S, Stannard C, Cole P, et al. Fentanyl for neuropathic pain in adults. *Cochrane Database Syst Rev* 2016; **10**: CD011605

15. Gaskell H, Derry S, Stannard C, Moore RA. Oxycodone for neuropathic pain in adults. *Cochrane Database Syst Rev* 2016; **7**: CD010692

16. Weisberg DF, Becker WC, Fiellin DA, Stannard C. Prescription opioid misuse in the United States and the United Kingdom: cautionary lessons. *Int J Drug Policy* 2014; **25**: 1124–30

17. Stoicea N, Costa A, Periel L, Uribe A, Weaver T, Bergese SD. Current perspectives on the opioid crisis in the US healthcare system: a comprehensive literature review. *Medicine (Baltimore)* 2019; **98**, e15425

18. Guy Jr GP, Zhang K, Bohm MK, et al. Vital signs: changes in opioid prescribing in the United States, 2006–2015. *MMWR Morb Mortal Wkly Rep* 2017; **66**: 697–704

19. Gomes T, Tadrous M, Mamdani MM, Paterson JM, Juurlink DN. The burden of opioid-related mortality in the United States. *JAMA Netw Open* 2018; **1**, e180217

20. Tibbs GR, Posson DJ, Goldstein PA. Voltage-gated ion channels in the PNS: novel therapies for neuropathic pain? *Trends Pharmacol Sci* 2016; **37**: 522–42

21. Santoro B, Shah MM. Hyperpolarization-activated cyclic nucleotide-gated channels as drug targets for neurological disorders. *Ann Rev Pharmacol Toxicol* 2020; **60**: 109–31

22. He JT, Li XY, Zhao X, Liu X. Hyperpolarization-activated and cyclic nucleotide-gated channel proteins as emerging new targets in neuropathic pain. *Rev Neurosci* 2019; **30**: 639–49

23. Melchiorre M, Del Lungo M, Guandalini L, et al. Design, synthesis, and preliminary biological evaluation of new isoform-selective f-current blockers. *J Med Chem* 2010; **53**: 6773–7

24. McClure KJ, Maher M, Wu N, et al. Discovery of a novel series of selective HCN1 blockers. *Bioorg Med Chem Lett* 2011; **21**: 5197–201

25. Tibbs GR, Rowley TR, Sanford RL, et al. HCN1 channels as targets for anesthetic and non-anesthetic propofol analogs in the amelioration of mechanical and thermal hyperalgesia in a mouse model of neuropathic pain. *J Pharmacol Exp Ther* 2013; **345**: 363–73

26. Resta F, Micheli L, Laurino A, et al. Selective HCN1 block as a strategy to control oxaliplatin-induced neuropathy. *Neuropharmacology* 2018; **131**: 403–13

27. Emery EC, Young GT, Berrocoso EM, Chen L, McNaughton PA. HCN2 ion channels play a central role in inflammatory and neuropathic pain. *Science* 2011; **333**: 1462–6

28. Tsantoulas C, Laínez S, Wong S, Mehta I, Vilar B, McNaughton PA. Hyperpolarization-activated cyclic nucleotide-gated 2 (HCN2) channels drive pain in mouse models of diabetic neuropathy. *Sci Transl Med* 2017; **9**, eaam6072

29. Stillitano F, Lonardo G, Zicha S, et al. Molecular basis of funny current (I_f) in normal and failing human heart. *J Mol Cell Cardiol* 2008; **45**: 289–99

30. Soltysinska E, Olesen SP, Christ T, et al. Transmural expression of ion channels and transporters in human nondiseased and end-stage failing hearts. *Pflugers Arch* 2009; **459**: 11–23

31. Chandler NJ, Greener ID, Tellez JO, et al. Molecular architecture of the human sinus node: insights into the function of the cardiac pacemaker. *Circulation* 2009; **119**: 1562–75

32. Chen S, Wang J, Siegelbaum SA. Properties of hyperpolarization-activated pacemaker current defined by coassembly of HCN1 and HCN2 subunits and basal modulation by cyclic nucleotide. *J Gen Physiol* 2001; **117**: 491–504

33. Chen X, Shu S, Bayliss DA. Suppression of I_h contributes to propofol-induced inhibition of mouse cortical pyramidal neurons. *J Neurophysiol* 2005; **94**: 3872–83

34. Joyce RL, Beyer NP, Vasilopoulos G, et al. Alkylphenol inverse agonists of HCN1 gating: H-bond propensity, ring saturation and adduct geometry differentially determine efficacy and potency. *Biochem Pharmacol* 2019; **163**: 493–508

35. Acuña MA, Yevenes GE, Ralvenius WT, et al. Phosphorylation state-dependent modulation of spinal glycine receptors alleviates inflammatory pain. *J Clin Invest* 2016; **126**: 2547–60

36. Kim JJ, Gharpure A, Teng J, et al. Shared structural mechanisms of general anaesthetics and benzodiazepines. *Nature* 2020; **585**: 303–8

37. Kim ED, Falzone ME, Tibbs GR, Ferrer ML, Goldstein PA, Nimigean CM. Perturbation of HCN1 response to small molecule modulation. *Biophys J* 2023; **122**: 519A–20A

38. Jo S, Kim T, Iyer VG, Im W. CHARMM-GUI: a web-based graphical user interface for CHARMM. *J Comput Chem* 2008; **29**: 1859–65

39. Jorgensen WL, Chandrasekhar J, Madura JD, Impey RW, Klein ML. Comparison of simple potential functions for simulating liquid water. *J Chem Phys* 1983; **79**: 926–35

40. Klauda JB, Venable RM, Freites JA, et al. Update of the CHARMM all-atom additive force field for lipids: validation on six lipid types. *J Phys Chem B* 2010; **114**: 7830–43

41. Vanommeslaeghe K, Hatcher E, Acharya C, et al. CHARMM general force field: a force field for drug-like molecules compatible with the CHARMM all-atom additive biological force fields. *J Comput Chem* 2010; **31**: 671–90

42. Abraham MJ, Murtola T, Schulz R, et al. GROMACS: high performance molecular simulations through multi-level parallelism from laptops to supercomputers. *SoftwareX* 2015; **1–2**: 19–25

43. Hoover WG. Canonical dynamics: equilibrium phase-space distributions. *Phys Rev A Gen Phys* 1985; **31**: 1695–7

44. Nosé S. A molecular dynamics method for simulations in the canonical ensemble. *Mol Phys* 1984; **52**: 255–68

45. Parrinello M, Rahman A. Polymorphic transitions in single crystals: a new molecular dynamics method. *J Appl Phys* 1981; **52**: 7182–90

46. Hess B, Bekker H, Berendsen HJC. LINCS: a linear constraint solver for molecular simulations. *J Comput Chem* 1997; **18**: 1463–72

47. Essmann U, Perera L, Berkowitz ML, Darden T, Lee H, Pedersen LG. A smooth particle mesh Ewald method. *J Chem Phys* 1995; **103**: 8577–93

48. Lee CH, MacKinnon R. Structures of the human HCN1 hyperpolarization-activated channel. *Cell* 2017; **168**: 111–120.e11

49. Wager TT, Hou X, Verhoest PR, Villalobos A. Moving beyond rules: the development of a central nervous system multiparameter optimization (CNS MPO) approach to enable alignment of druglike properties. *ACS Chem Neurosci* 2010; **1**: 435–49

50. Wager TT, Hou X, Verhoest PR, Villalobos A. Central nervous system multiparameter optimization desirability: application in drug discovery. *ACS Chem Neurosci* 2016; **7**: 767–75

51. Dhillon S, Gill K. Basic pharmacokinetics. In: Dhillon S, Kostrzewski AJ, editors. *Clinical pharmacokinetics*. London: Pharmaceutical Press; 2006. p. 280

52. Hall C, Lueshen E, Mošat A, Linninger AA. Interspecies scaling in pharmacokinetics: a novel whole-body physiologically based modeling framework to discover drug biodistribution mechanisms *in vivo*. *J Pharm Sci* 2012; **101**: 1221–41

53. Deuis JR, Dvorakova LS, Vetter I. Methods used to evaluate pain behaviors in rodents. *Front Mol Neurosci* 2017; **10**: 284

54. Decosterd I, Woolf CJ. Spared nerve injury: an animal model of persistent peripheral neuropathic pain. *Pain* 2000; **87**: 149–58

55. Wang LX, Wang ZJ. Animal and cellular models of chronic pain. *Adv Drug Deliv Rev* 2003; **55**: 949–65

56. Colburn RW, Lubin ML, Stone Jr DJ, et al. Attenuated cold sensitivity in TRPM8 null mice. *Neuron* 2007; **54**: 379–86

57. Cheng VY, Martin LJ, Elliott EM, et al. α5GABA$_A$ receptors mediate the amnestic but not sedative-hypnotic effects of the general anesthetic etomidate. *J Neurosci* 2006; **26**: 3713–20

58. Borer JS, Le Heuzey JY. Characterization of the heart rate-lowering action of ivabradine, a selective i$_f$ current inhibitor. *Am J Ther* 2008; **15**: 461–73

59. Ferrari R, Camici PG, Crea F, et al. Expert consensus document: a 'diamond' approach to personalized treatment of angina. *Nat Rev Cardiol* 2018; **15**: 120–32

60. Prus AJ, James JR, Rosecrans JA. Conditioned place preference. In: Buccafusco JJ, editor. *Methods of behavior analysis in neuroscience*. 2nd edition. Boca Raton, FL: CRC Press/Taylor & Francis; 2009. Chapter 4. Available from: https://www. ncbi.nlm.nih.gov/books/NBK5229/

61. Schneider W, Bortfeld T, Schlegel W. Correlation between CT numbers and tissue parameters needed for Monte Carlo simulations of clinical dose distributions. *Phys Med Biol* 2000; **45**: 459–78

62. Lloyd BA. Tissue properties—density. Zurich, Switzerland: IT'IS Foundation. Available from https://itis.swiss/virtual-population/tissue-properties/database/density/ (accessed 20 March 2023).

63. Khelashvili G, Menon AK. Phospholipid scrambling by G protein-coupled receptors. *Annu Rev Biophys* 2022; **51**: 39–61

64. Chen S, Wang J, Zhou L, George MS, Siegelbaum SA. Voltage sensor movement and cAMP binding allosterically regulate an inherently voltage-independent closed-open transition in HCN channels. *J Gen Physiol* 2007; **129**: 175–88

65. Banks WA. Characteristics of compounds that cross the blood-brain barrier. *BMC Neurol* 2009; **9**: S3

66. Luo L, Chang L, Brown SM, et al. Role of peripheral hyperpolarization-activated cyclic nucleotide-modulated channel pacemaker channels in acute and chronic pain models in the rat. *Neuroscience* 2007; **144**: 1477–85

67. Jiang YQ, Xing GG, Wang SL, et al. Axonal accumulation of hyperpolarization-activated cyclic nucleotide-gated cation channels contributes to mechanical allodynia after peripheral nerve injury in rat. *Pain* 2008; **137**: 495–506

68. Jiang YQ, Sun Q, Tu HY, Wan Y. Characteristics of HCN channels and their participation in neuropathic pain. *Neurochem Res* 2008; **33**: 1979–89

69. Nirogi R, Goura V, Shanmuganathan D, Jayarajan P, Abraham R. Comparison of manual and automated filaments for evaluation of neuropathic pain behavior in rats. *J Pharmacol Toxicol Methods* 2012; **66**: 8–13

70. Hargreaves K, Dubner R, Brown F, Flores C, Joris J. A new and sensitive method for measuring thermal nociception in cutaneous hyperalgesia. *Pain* 1988; **32**: 77–88

71. Baliki MN, Geha PY, Apkarian AV, Chialvo DR. Beyond feeling: chronic pain hurts the brain, disrupting the default-mode network dynamics. *J Neurosci* 2008; **28**: 1398–403

72. Sartiani L, Mannaioni G, Masi A, Novella Romanelli M, Cerbai E. The hyperpolarization-activated cyclic nucleotide-gated channels: from biophysics to pharmacology of a unique family of ion channels. *Pharmacol Rev* 2017; **69**: 354–95

73. Shi W, Wymore R, Yu H, et al. Distribution and prevalence of hyperpolarization-activated cation channel (HCN) mRNA expression in cardiac tissues. *Circ Res* 1999; **85**: e1–6

74. Herrmann S, Layh B, Ludwig A. Novel insights into the distribution of cardiac HCN channels: an expression study in the mouse heart. *J Mol Cell Cardiol* 2011; **51**: 997–1006

75. Baruscotti M, Barbuti A, Bucchi A. The cardiac pacemaker current. *J Mol Cell Cardiol* 2010; **48**: 55–64

76. Huang X, Yang P, Yang Z, Zhang H, Ma A. Age-associated expression of HCN channel isoforms in rat sinoatrial node. *Exp Biol Med (Maywood)* 2016; **241**: 331–9

77. Notomi T, Shigemoto R. Immunohistochemical localization of I$_h$ channel subunits, HCN1–4, in the rat brain. *J Comp Neurol* 2004; **471**: 241–76

78. Yamakura T, Lewohl JM, Harris RA. Differential effects of general anesthetics on G protein-coupled inwardly rectifying and other potassium channels. *Anesthesiology* 2001; **95**: 144–53

79. Minami K, Sudo Y, Shiraishi S, Seo M, Uezono Y. Analysis of the effects of anesthetics and ethanol on μ-opioid receptor. *J Pharmacol Sci* 2010; **112**: 424–31

80. Momin A, Cadiou H, Mason A, McNaughton PA. Role of the hyperpolarization-activated current I$_h$ in somatosensory neurons. *J Physiol* 2008; **586**: 5911–29

81. Tsantoulas C. Emerging potassium channel targets for the treatment of pain. *Curr Opin Support Palliat Care* 2015; **9**: 147–54

82. Lee MC, Bond S, Wheeler D, et al. A randomised, double-blind, placebo-controlled crossover trial of the influence of the HCN channel blocker ivabradine in a healthy volunteer pain model: an enriched population trial. *Pain* 2019; **160**: 2554–65

83. Bernard Healey SA, Scholtes I, Abrahams M, McNaughton PA, Menon DK, Lee MC. Role of hyperpolarization-activated cyclic nucleotide-gated ion channels in neuropathic pain: a proof-of-concept study of ivabradine in patients with chronic peripheral neuropathic pain. *Pain Rep* 2021; **6**: e967

84. Shiers S, Klein RM, Price TJ. Quantitative differences in neuronal subpopulations between mouse and human dorsal root ganglia demonstrated with RNAscope in situ hybridization. *Pain* 2020; **161**: 2410–24

85. Hou B, Chen H, Qu X, Lin X, Luo F, Li C. Characteristics of hyperpolarization-activated cyclic nucleotide-gated channels in dorsal root ganglion neurons at different ages and sizes. *Neuroreport* 2015; **26**: 981–7

86. North RY, Li Y, Ray P, et al. Electrophysiological and transcriptomic correlates of neuropathic pain in human dorsal root ganglion neurons. *Brain* 2019; **142**: 1215–26

87. Young GT, Gutteridge A, Fox HD, et al. Characterizing human stem cell-derived sensory neurons at the single-cell level reveals their ion channel expression and utility in pain research. *Mol Ther* 2014; **22**: 1530–43

88. Lainez S, Tsantoulas C, Biel M, McNaughton PA. HCN3 ion channels: roles in sensory neuronal excitability and pain. *J Physiol* 2019; **597**: 4661–75

89. Moosmang S, Stieber J, Zong X, Biel M, Hofmann F, Ludwig A. Cellular expression and functional characterization of four hyperpolarization-activated pacemaker channels in cardiac and neuronal tissues. *Eur J Biochem* 2001; **268**: 1646–52

90. Kouranova EV, Strassle BW, Ring RH, Bowlby MR, Vasilyev DV. Hyperpolarization-activated cyclic nucleotide-gated channel mRNA and protein expression in large versus small diameter dorsal root ganglion neurons: correlation with hyperpolarization-activated current gating. *Neuroscience* 2008; **153**: 1008–19

91. DiFrancesco D. A brief history of pacemaking. *Front Physiol* 2019; **10**: 1599

92. Li N, Csepe TA, Hansen BJ, et al. Molecular mapping of sinoatrial node HCN channel expression in the human heart. *Circ Arrhythm Electrophysiol* 2015; **8**: 1219–27

93. Greener ID, Monfredi O, Inada S, et al. Molecular architecture of the human specialised atrioventricular conduction axis. *J Mol Cell Cardiol* 2011; **50**: 642–51

94. Yokoyama R, Kinoshita K, Hata Y, et al. A mutant HCN4 channel in a family with bradycardia, left bundle branch block, and left ventricular noncompaction. *Heart Vessels* 2018; **33**: 802–19

95. Verkerk AO, Wilders R. Pacemaker activity of the human sinoatrial node: an update on the effects of mutations in HCN4 on the hyperpolarization-activated current. *Int J Mol Sci* 2015; **16**: 3071–94

96. Staines R. Merck & Co pens $340m pain drug deal with KCL and Wellcome. *Pharmaphorum* 2019. Available from, https://pharmaphorum.com/news/merck-co-pens-340m-pain-drug-deal-with-kcl-and-wellcome. [Accessed 27 March 2023]

97. Cook DC, Goldstein PA. Non-canonical molecular targets for novel analgesics: intracellular calcium and HCN channels. *Curr Neuropharmacol* 2021; **19**: 1937–51

98. Gardiner SM, Kemp PA, March JE, Bennett T. Acute and chronic cardiac and regional haemodynamic effects of the novel bradycardic agent, S16257, in conscious rats. *Br J Pharmacol* 1995; **115**: 579–86

99. DiFrancesco D. Funny channels in the control of cardiac rhythm and mode of action of selective blockers. *Pharmacol Res* 2006; **53**: 399–406

100. Fox K, Ford I, Steg PG, Tendera M, Ferrari R. Ivabradine for patients with stable coronary artery disease and left-ventricular systolic dysfunction (BEAUTIFUL): a randomised, double-blind, placebo-controlled trial. *Lancet* 2008; **372**: 807–16

101. Swedberg K, Komajda M, Böhm M, et al. Ivabradine and outcomes in chronic heart failure (SHIFT): a randomised placebo-controlled study. *Lancet* 2010; **376**: 875–85

102. U.S. Food & Drug Administration. Novel drug approvals for 2015 2015. Available from https://www.fda.gov/drugs/new-drugs-fda-cders-new-molecular-entities-and-new-therapeutic-biological-products/novel-drug-approvals-2015 (accessed 21 February 2023).

103. European Medicines Agency. *Procoralan* 2005. Available from, https://www.ema.europa.eu/en/medicines/human/EPAR/procoralan#authorisation-details-section. [Accessed 21 February 2023]

104. Luszczki JJ, Prystupa A, Andres-Mach M, Marzeda E, Florek-Luszczki M. Ivabradine (a hyperpolarization activated cyclic nucleotide-gated channel blocker) elevates the threshold for maximal electroshock-induced tonic seizures in mice. *Pharmacol Rep* 2013; **65**: 1407–14

105. Sawicka KM, Zaluska K, Wawryniuk A, et al. Ivabradine attenuates the anticonvulsant potency of lamotrigine, but not that of lacosamide, pregabalin and topiramate in the tonic-clonic seizure model in mice. *Epilepsy Res* 2017; **133**: 67–70

106. Sawicka KM, Wawryniuk A, Zwolak A, et al. Influence of ivabradine on the anticonvulsant action of four classical antiepileptic drugs against maximal electroshock-induced seizures in mice. *Neurochem Res* 2017; **42**: 1038–43

107. Cavalcante TMB, De Melo JMAJ, Lopes LB, et al. Ivabradine possesses anticonvulsant and neuroprotective action in mice. *Biomed Pharmacother* 2019; **109**: 2499–512

108. Kharouf Q, Pinares-Garcia P, Romanelli MN, Reid CA. Testing broad-spectrum and isoform-preferring HCN channel blockers for anticonvulsant properties in mice. *Epilepsy Res* 2020; **168**, 106484

109. Iacone Y, Morais TP, David F, et al. Systemic administration of ivabradine, a hyperpolarization-activated cyclic nucleotide-gated channel inhibitor, blocks spontaneous absence seizures. *Epilepsia* 2021; **62**: 1729–43

110. Cacheaux LP, Topf N, Tibbs GR, et al. Impairment of hyperpolarization-activated, cyclic nucleotide-gated channel function by the intravenous general anesthetic propofol. *J Pharmacol Exp Ther* 2005; **315**: 517–25

111. Del Lungo M, Melchiorre M, Guandalini L, et al. Novel blockers of hyperpolarization-activated current with isoform selectivity in recombinant cells and native tissue. *Br J Pharmacol* 2012; **166**: 602–16

112. Brewster AL, Bernard JA, Gall CM, Baram TZ. Formation of heteromeric hyperpolarization-activated cyclic nucleotide-gated (HCN) channels in the hippocampus is regulated by developmental seizures. *Neurobiol Dis* 2005; **19**: 200–7

113. Zha Q, Brewster AL, Richichi C, Bender RA, Baram TZ. Activity-dependent heteromerization of the hyperpolarization-activated, cyclic-nucleotide gated (HCN) channels: role of *N*-linked glycosylation. *J Neurochem* 2008; **105**: 68–77

114. Gao LL, McMullan S, Djouhri L, Acosta C, Harper AA, Lawson SN. Expression and properties of hyperpolarization-activated current in rat dorsal root ganglion neurons with known sensory function. *J Physiol* 2012; **590**: 4691–705

115. Raja SN, Ringkamp M, Guan Y, Campbell JN. John J. Bonica Award Lecture: peripheral neuronal hyperexcitability: the "low-hanging" target for safe therapeutic strategies in neuropathic pain. *Pain* 2020; **161**: S14–26

Handling Editor: Nadine Attal